

1 **Higher sediment redistribution rates related to burrowing animals than previously assumed as revealed
2 by Time-Of-Flight based monitoring**

3
4 *Paulina Grigusova¹, Annegret Larsen², Sebastian Achilles¹, Roland Brandl³, Camilo del Rio^{4,5}, Nina Farwig⁶,
5 Diana Kraus⁶, Leandro Paulino⁷, Patricio Plischoff^{4,8,9}, Kirstin Übernickel¹⁰, Jörg Bendaix¹*

6
7

8 ¹ Laboratory for Climatology and Remote Sensing, Department of Geography, University of Marburg, 35037
9 Marburg, Germany; paulina.grigusova@staff.uni-marburg.de (P.G.); bendix@geo.uni-marburg.de (J.B.)

10 ² Soil Geography and Landscape, Department of Environmental Sciences,
11 Wageningen University & Research, 6700 AA Wageningen, The Netherlands; annegret.larsen@wur.nl

12 ³ Animal Ecology, Department of Biology, University of Marburg, 35032 Marburg, Germany;
13 brandl@biologie.uni-marburg.de

14 ⁴ Facultad de Historia, Geografía y Ciencia Política, Instituto de Geografía, Pontificia Universidad Católica de
15 Chile, 782-0436 Santiago, Chile; plischoff@uc.cl; cdelriol@uc.cl

16 ⁵ Centro UC Desierto de Atacama, Pontificia Universidad Católica de Chile, 782-0436 Santiago, Chile;
17 cdelriol@uc.cl

18 ⁶ Conservation Ecology, Department of Biology, University of Marburg, 35047 Marburg, Germany;
19 diana.kraus@biologie.uni-marburg.de (D.K.); nina.farwig@biologie.uni-marburg.de (N.F.)

20 ⁷ Facultad de Agronomía, Universidad de Concepción, 3780000 Chillán, Chile; l paulino@udec.cl

21 ⁸ Facultad de Ciencias Biológicas, Departamento de Ecología, Pontificia Universidad Católica de Chile, 8331150
22 Santiago, Chile; plischoff@uc.cl

23 ⁹ Center of Applied Ecology and Sustainability (CAPES), Pontificia Universidad Católica de Chile, 8331150
24 Santiago, Chile; plischoff@uc.cl

25 ¹⁰ Earth System Dynamics, Department of Geosciences, University of Tübingen, 72076 Tübingen, Germany;
26 kirstin.uebernickel@uni-tuebingen.de

27

28 *Corresponding author:*

29 Paulina Grigusova

30 paulina.grigusova@staff.uni-marburg.de

31

32

33

34

35

36

37

38

39

40

41 **Abstract**

42 Burrowing animals influence surface microtopography and hillslope sediment redistribution, but changes often
43 remain undetected due to a lack of automated high resolution field monitoring techniques. In this study, we
44 present a new approach to quantify microtopographic variations and surface changes caused by burrowing
45 animals and rainfall-driven erosional processes applied to remote field plots in arid and Mediterranean Chile.
46 We compared the mass balance of redistributed sediment between burrow and burrow embedding area,
47 quantified the cumulative sediment redistribution caused by animals and rainfall, and upscaled the results to a
48 hillslope scale. The newly developed instrument, a Time-of-Flight camera, showed a very good detection
49 accuracy. The animal-caused cumulative sediment excavation was $14.6 \text{ cm}^3 \text{ cm}^{-2} \text{ year}^{-1}$ in the Mediterranean,
50 and $16.4 \text{ cm}^3 \text{ cm}^{-2} \text{ year}^{-1}$ in the arid climate zone. The rainfall-caused cumulative sediment erosion within
51 burrows was higher ($10.4 \text{ cm}^3 \text{ cm}^{-2} \text{ year}^{-1}$) in the Mediterranean than the arid climate zone ($1.4 \text{ cm}^3 \text{ cm}^{-2} \text{ year}^{-1}$).
52 Daily sediment redistribution during rainfall within burrow areas were up to 350% / 40% higher in the
53 mediterranean / arid zone compared to burrow embedding areas, and much higher than previously reported in
54 studies which were not based on continuous microtopographic monitoring. 38% of the sediment eroding from
55 burrows accumulated within the burrow entrance while 62% was incorporated into hillslope sediment flux, which
56 exceeds previous estimations two-fold. Animals burrowed between on average 1.2 – 2.3 times a month, and
57 the burrowing intensity increased after rainfall. This revealed a newly detected feedback mechanism between
58 rainfall, erosion, and animal burrowing activity, likely leading to an underestimation of animal-triggered hillslope
59 sediment flux in wetter climates. Our findings hence show that the rate of sediment redistribution due to animal
60 burrowing is climate dependant, and that animal burrowing plays a larger than previously expected role in
61 hillslope sediment redistribution. Subsequently, animal burrowing activity should be incorporated into soil
62 erosion and landscape evolution models that rely on soil processes but do not yet include animal-induced
63 surface processes on microtopographical scales in their algorithms.

64

65 **Keywords:** Biogeomorphology, bioturbation, sediment transport, burrowing animals, rainfall, Time-of-Flight
66 camera, Chile

67

68

69

70

71

72

73

74

75

76

77

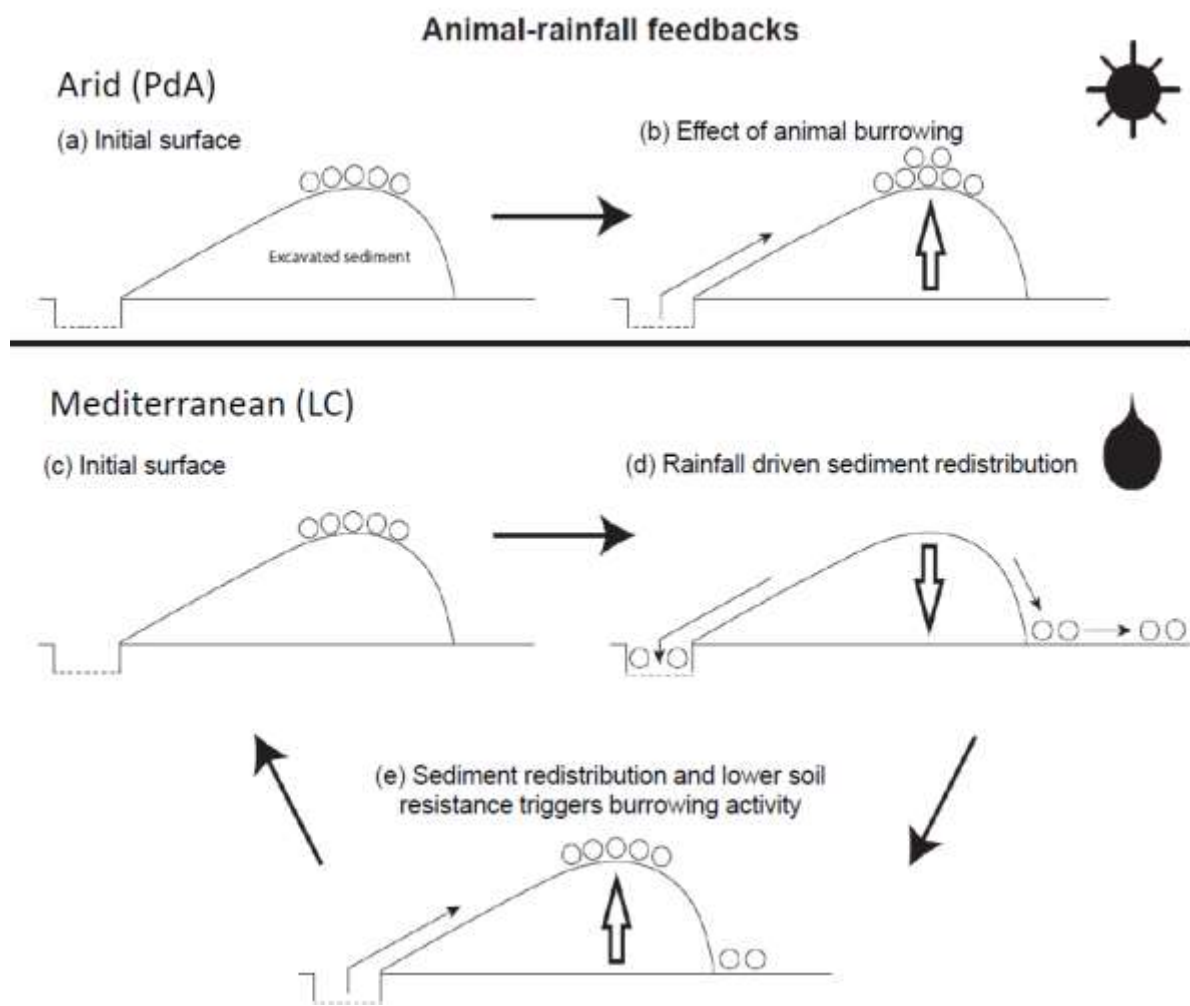
78

79

80

81
82
83
84
85

86 **Graphical abstract**



87
88

89 **1. Introduction**

90 Animal burrowing activity affects surface microtopography (Reichman und Seabloom 2002; Kinlaw
91 und Grasmueck 2012), surface roughness (Yair 1995; Jones et al. 2010; Hancock und Lowry 2021), and soil
92 physical properties (Ridd 1996; Yair 1995; Hall et al. 1999; Reichman und Seabloom 2002; Hancock und Lowry
93 2021; Coombes 2016; Larsen et al. 2021; Corenblit et al. 2021). Previous studies estimated both positive as
94 well as negative impacts of burrowing animals on sediment redistribution rates. These studies relied on
95 applying tests under laboratory conditions using rainfall simulators, conducting several field campaigns weeks
96 to months apart, or by measuring the volume of excavated or eroded sediment in the field using instruments
97 such as erosion pins, splash boards, or simple rulers (Imeson und Kwaad 1976; Reichman und Seabloom
98 2002; Wei et al. 2007; Le Hir et al. 2007; Li et al. 2018; Li et al. 2019b; Li et al. 2019c; Voiculescu et al. 2019;
99 Chen et al. 2021; Übernickel et al. 2021b; Li et al. 2019a). Although burrowing animals are generally seen as
100 ecosystem engineers (Gabet et al. 2003; Wilkinson et al. 2009), their role in soil erosion in general, and for
101 numerical soil erosion models in particular, is to date limited to predictions of burrow locations and particle
102 mixing (Black und Montgomery 1991; Meysman et al. 2003; Yoo et al. 2005; Schiffers et al. 2011). The complex
103 interaction of sediment excavation and accumulation, and erosion processes at the burrow and hillslope scale
104 are not yet included in earth-surface-models.

105 The reason for this knowledge gap is that previous studies have not provided data on low magnitude
106 but frequently occurring sediment redistribution due to a lack of spatio-temporal high-resolution
107 microtopographic surface monitoring techniques which can also measure continuously in the field. Field
108 experiments with, for example, rainfall simulators can unveil processes but cannot cover the time-dependant
109 natural dynamics of sediment redistribution. When using erosion pins or splash boards, the sites had to be
110 revisited each time and the data were thus obtained only sporadically (Imeson und Kwaad 1976; Hazelhoff et
111 al. 1981; Richards und Humphreys 2010). This limited all previous studies in their explanatory power, because
112 biotic-driven processes are typically characterised by small quantity and a frequent re-occurrence (Larsen et
113 al. 2021). It is hence likely that previous studies based on non-continuously conducted measurements or
114 rainfall experiments underestimated the role of burrowing animals on rates of hillslope sediment flux.

115 High-resolution, ground-based imaging sensing techniques have the potential to overcome limitations
116 of previous surface monitoring techniques. Terrestrial laser scanner systems have been shown to be a suitable
117 tool for the estimation of sediment redistribution and erosion processes (Nasermoaddeli und Pasche 2008;
118 Afana et al. 2010; Eltner et al. 2016a; Eltner et al. 2016b; Longoni et al. 2016). However, these instruments
119 are expensive and labour-intensive. Hence, a simultaneous, continuous, and automated monitoring of several
120 animal burrows is for this reason not possible. Time-lapse photogrammetry is a low-cost (up to 5000 USD),
121 topographic monitoring technique, which can be applied at variable observation distances and scales (e.g.
122 (James und Robson 2014; Galland et al. 2016; Eltner et al. 2017; Mallalieu et al. 2017; Kromer et al. 2019;
123 Blanch et al. 2021). However, several cameras are needed to monitor the surface under various angles, which
124 makes the field installation difficult and yields the large potential to disturb the animals and lead to behavioural
125 changes.

126 Another high resolution surface monitoring technique is based on Time-of-Flight (ToF) technology.
127 ToF-based cameras illuminate the targeted object with a light source for a known amount of time and then
128 estimate the distance between the camera and the object by measuring the time needed for the reflected light
129 to reach the camera sensor (Sarbolandi et al. 2018). ToF cameras exhibit lower spatial resolution and aerial
130 coverage compared to time-lapse photogrammetry. But, the technique also has several advantages: as an

131 active remote sensing tool it is able to monitor surface change at night, the processing is less complex
132 compared to photogrammetry because the distance values are immediately received in a local coordinate
133 system, and the field installation is much smaller and less invasive. ToF offers hence a new possibility for
134 surface monitoring, as a technique for a cost-effective, high-resolution monitoring of sediment redistribution
135 (Eitel et al. 2011; Hänsel et al. 2016), which can be achieved by a simple installation of only one device in the
136 field.

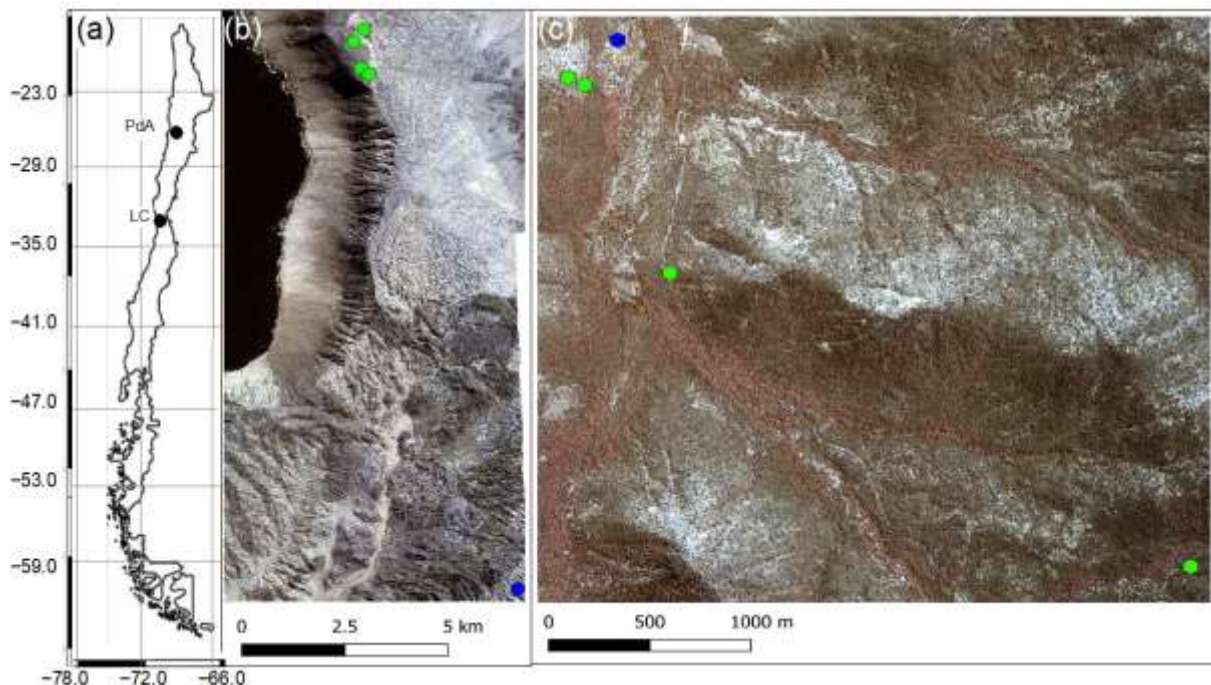
137 In this study we developed, tested and applied a cost-effective Time-of-Flight camera for automated
138 monitoring of the rainfall and burrowing animal-driven sediment redistribution of burrows and burrow
139 embedding areas with a high temporal (four times a day) and spatial (6 mm) resolution. For this, we equipped
140 several plots in remote field study sites in the Chilean arid and mediterranean climate zone. The selected field
141 sites had a variable rainfall regime and sunlight exposure, and were all affected by burrowing activity
142 (Grigusova et al. 2021). After 7 month of field monitoring including wet and dry season, we estimated burrowing
143 intensity and its dependence on rainfall. Then, we quantified the daily sediment redistribution within the burrow
144 and its embedding area, which enabled us to better understand the impacts of animal burrowing activity, and
145 rainfall, on the local sediment redistribution. This allowed us to quantify the volume of burrow sediment which
146 was incorporated into the hillslope sediment flux. Finally, we upscaled sediment redistribution rates to the
147 entire hillslope.

148

149 **2. Study area**

150 Our study sites were located in the Chilean Coastal Cordillera in two climate zones (Fig. 1): in the National
151 Park Pan de Azúcar (further as Pan de Azúcar or PdA) and the National Park La Campana (further as La
152 Campana or LC). The Las Lomitas site in PdA is located in the arid climate zone of the Atacama Desert with a
153 precipitation rate of 12 mm year⁻¹, and it has a mean annual temperature of 16.8 °C (Übernickel et al. 2021a).
154 Here, the vegetation cover is below 5%, and it is dominated by small desert shrubs, several species of cacti
155 (*Eulychnia breviflora*, *Copiapoa atacamensis*) and biocrusts (Lehnert et al. 2018). LC is located in the
156 mediterranean climate zone with a precipitation rate of 367 mm year⁻¹ and a mean annual temperature of
157 14.1 °C (Übernickel et al. 2021a). LC is dominated by an evergreen sclerophyllous forest with endemic palm
158 trees, *Jubaea chilensis*. Both research sites have a granitic rock base, and the dominating soil texture is sandy
159 loam (Bernhard et al. 2018). In PdA, the study setup consisted of one north-facing and one south-facing
160 hillslope. The hillslope inclinations were ~20°, and a climate station was located ~15 km from the camera sites.
161 In LC, the setup consisted of two north-facing and one south-facing hillslopes. The hillslope inclinations were
162 ~25°, and a climate station was located ~250 m from the south-facing hillslope (Übernickel et al. 2021a).

163



164

165 **Figure 1.** Location of the cameras and climate stations on which this study was based. Black points show the
 166 location of the research sites in Chile. The green points represent the camera plots, and the blue points the
 167 climate stations: (a) Location of study sites in Chile: PdA stands for Pan de Azúcar, LC for La Campana; (b)
 168 Study setup in Pan de Azúcar; (c) Study setup in LC. The background images in (b) and (c) are orthophotos
 169 created from WorldView-2 data from 19 July 2019. For exact latitude and longitude see Table A2.

170

171 2.1 Local burrowing animals

172 In order to assess which animal species burrowed at both study sites, we adapted a two-step approach. First,
 173 we used motion-activated camera traps to capture animals during the borrowing process at our field sites.
 174 Then, we complimented the list of identified species by a literature review. We found that the most common
 175 vertebrate animal species which burrow in PdA were carnivores of the family Canidae (*Lycalopex culpaeus*,
 176 *Lycalopex griseus*) as well as rodents of the families Abrocomidae (*Abrocoma bennetti*), Chinchillidae
 177 (*Lagidium viscacia*), Cricetidae (*Abrothrix andinus*, *Phyllotis xanthopygus*, *Phyllotis limatus*, *Phyllotis darwini*)
 178 and Octogontidae (Cerquiera 1985, Jiménez et al. 1992, Übernickel et al. 2021) (Table 1). In LC, the most
 179 common burrowing vertebrate animal species were the carnivores of the family Canidae, Lagomorpha of the
 180 family Leporidae (*Oryctolagus cuniculus*), and rodents of the families Cricetidae (*Abrothrix longipilis*, *Abrothrix*
 181 *olivaceus*, *Phyllotis darwini*), Muridae (*Mus musculus*) and Octogontidae (*Octodon degus*, *Spalacopus cyanus*)
 182 (Muñoz-Pedreros et al. 2018, Übernickel et al. 2021) (Table 1. The motion-activated camera traps recorded
 183 several burrowing animals which all agreed with the list of burrowing vertebrate animals collected from
 184 literature: *Lycalopex culpaeus*, *Oryctolagus cuniculus* and *Abrocoma bennetti*) (Figure 2)

185

186 **Table 1.** Most common burrowing animals in the study sites. The list includes both, animal species recorded
 187 with our motion-activated wildlife traps and those from the review by Übernickel et al. 2021, Cerquiera 1985,
 188 Jiménez et al. 1992, Muñoz-Pedreros et al. 2018). “X” indicates at which site the species can be found.

Order	Family	Species	Common name	Site	
				PdA	LC

Carnivora	Canidae	<i>Lycalopex culpaeus</i>	Culpeo	X	X
Carnivora	Canidae	<i>Lycalopex griseus</i>	South-American grey fox	X	X
Carnivora	Methitidae	<i>Conepatus chinga</i>	Molina's Hog nosed skunk		X
Lagomorpha	Leporidae	<i>Oryctolagus cuniculus</i>	European rabbit		X
Rodentia	Abrocomidae	<i>Abrocoma bennetti</i>	Bennett's chinchilla rat	X	X
Rodentia	Chinchillidae	<i>Lagidium viscacia</i>	Southern mountain vischacha	X	
Rodentia	Cricetidae	<i>Abrothrix andinus</i>	Andean grass mouse	X	
Rodentia	Cricetidae	<i>Abrothrix longipilis</i>	Long-haired mouse	X	X
Rodentia	Cricetidae	<i>Abrothrix olivaceus</i>	Olive grass mouse	X	X
Rodentia	Cricetidae	<i>Phyllotis darwini</i>	Darwin's leaf-eared mouse	X	X
Rodentia	Cricetidae	<i>Phyllotis xanthopygus</i>	Yellow leaf-eared mouse	X	
Rodentia	Cricetidae	<i>Phyllotis limatus</i>	Lima leaf-eared mouse	X	
Rodentia	Muridae	<i>Mus musculus</i>	Common house mouse	X	X
Rodentia	Octogontidae	<i>Octodon degus</i>	Degu (rat)	X	X
Rodentia	Octogontidae	<i>Spalacopus cyanus</i>	Coruro (rat)	X	X

189

190



191

192 **Figure 2.** Examples of burrowing vertebrate animals recorded by motion-activated camera traps. (a) Set-up of
193 motion-activated camera trap. (b) and (c) European rabbit (*Oryctolagus cuniculus*). (d) and (e) Culpeo
194 (*Lycalopex culpaeus*). (f) Bennett's chinchilla rat (*Abrocoma bennetti*). The yellow box highlights the position
195 of the animal on the photo. Photo courtesy: Diana Kraus.

196

197 **3. Methodology**

198 **3.1 Time-of-Flight (ToF) principle**

199 A Time-of-Flight-based camera illuminates an object with a light source, usually in a non-visible
200 spectrum, such as near-infrared, for a precise length of time. ToF cameras rely on the principle of measuring
201 the phase shift, with different options to modulate the light source to be able to measure the phase shift. The
202 here employed cameras used pulse-based modulation, meaning the light pulse was first emitted by the
203 camera, then reflected from the surface, and finally measured by the camera using two temporary windows.

204 The opening of the first window is synchronized with the pulse emission i.e. the receiver opens the window
205 with the same Δt as the emitted pulse. Then, the second window is opened, for the same duration Δt , which is
206 synchronised with the closing of the first window. The first temporary window thus measures the incoming
207 reflected light while the light pulse is also still emitting from the camera. The second temporary window
208 measures the incoming reflected light when no pulse is emitting from the camera. The captured photon number
209 (i.e. measured by electrical charge) in both windows can be related according to equation 1 and the distance
210 from the camera to the object can then be calculated as follows:

211
$$d = \frac{1}{2} * c * t * \left(\frac{g_1}{g_1 + g_2} \right) \quad . \quad (1)$$

212 In Eq. (1), d (m) is the distance from the camera to the object, c (m s^{-1}) is the speed of light ($299,792,458 \text{ m s}^{-1}$), t (s) is the overall time of the illumination and measurement, g_1 is the ratio of the reflected photons to all
213 photons accumulated in the first window, and g_2 the ratio of the reflected photons to all photons accumulated
214 in the second window (Sarbolandi et al. 2018; Li 2014).

215 The sensor in our camera came from Texas Instruments and the data scan contained information on
216 320 x 240 points. The camera field of view (FOV) and the spatial resolution of the scans depended on the
217 height of the camera above the surface and camera orientation. The distance was calculated for every point,
218 and the object was saved in binary format as a collection of 3D points with x -, y - and z -coordinates. The point
219 clouds taken by the camera were transformed from the binary format to an ASCII format. Each point in the
220 point cloud was assigned to an x -, y - and z -coordinate. The coordinates were distributed within a three-
221 dimensional Euclidian space, with the point at the camera nadir (the centre of the camera sensor) being the
222 point of origin of the 3D Cartesian coordinate system. x - and y -coordinates describe the distance to the point
223 of origin (m). z -coordinate describes the distance (m) from the object to the camera. The lowest point of the
224 scanned surface thus has the highest z -coordinate value.

225

226 3.2 Data processing

227 The distortion caused by the hillslope and the camera angle was corrected for each point cloud as
228 follows:

229
$$z_{cor} = z_{uncor} - \tan(\alpha + \beta) * (y_i - y_0) \quad . \quad (2)$$

230 In Eq. (2), z_{cor} is the corrected distance (m) between the camera and surface (m), z_{uncor} is the uncorrected z -
231 coordinate (m), α is the tilt angle of the camera ($^\circ$), β is the surface inclination ($^\circ$), and y_i (m) is the distance
232 between each point, and the point with i) an y -coordinate = 0 and ii) the same x -coordinate as the respective
233 point. The most frequent errors were identified and treated as follows. Due to the ambient light reaching the
234 camera sensor, the z -coordinate values of some of the points were incorrect (scattering error). To remove this
235 error, a threshold value was calculated for each point cloud:

236
$$\Omega = \text{mean}_{zcor-coordinates} \pm \text{sd}_{zcor-coordinates} \quad . \quad (3)$$

237 In Eq. (3), Ω is the threshold value, $\text{mean}_{zcor-coordinates}$ is the average value, and $\text{sd}_{zcor-coordinates}$ is the standard
238 deviation of the corrected z -coordinates (m). Then, all points with a z -coordinate above and below this value
239 were deleted. Point clouds with more than 50% of points above the threshold value Ω were also not considered
240 for further processing. A drift error occurred when the z -coordinate values of around one-third of the point
241 clouds decreased by several centimetres from one point cloud to another. Here, the average z -coordinate of
242 ten point clouds before and after the drift were calculated, and the difference was added to z -coordinates of

244 the points affected by the drift. The corrected height values were then transformed into a digital surface model
245 (DSM).

246

247 **3.3 Accuracy of the ToF cameras**

248 The accuracy of the ToF camera was tested under laboratory conditions by recreating similar surface
249 conditions as in the field (sloping surface, covered by sediment). An artificial mound using sediment extracted
250 from a riverbank in central Germany was used, mimicking a mound created by a burrowing animal. During the
251 test, the camera was installed 100 cm above the surface. The camera FOV was 3 m² and the scan spatial
252 resolution was 6 mm. The surface was scanned twice by the ToF camera. Then 100 – 450 cm³ of sediment
253 was manually extracted from the mound. The volume of the extracted sediment was measured by a measuring
254 cup. After extraction, the surface was again scanned twice by the camera. The experiment was repeated 45
255 times with varying amounts of extracted sediment. The scans were transformed to point clouds in VoxelViewer-
256 0.9.10, and the point clouds were corrected according to Eq. (2) and (3). The z-coordinates of the two point
257 clouds before and two point clouds after the extraction were averaged. The standard deviation of the z-
258 coordinate of the two scans was 0.06 cm. Figure A1 shows the spatially distributed standard deviation. The
259 deviation increases from the centre towards the corners of the scan. The mound was outlined and only the
260 points representing the mound were used in the further analysis. The point clouds were then transformed into
261 DSMs, and the differences between the time steps were calculated. A scan was taken of a smooth surface
262 (linoleum floor) and a point cloud was created from the data. Then, we fitted a plane into the point cloud and
263 calculated the distance between the plane and the camera sensor. The standard variation (0.17 cm) in the
264 distance measurements was saved. Solely, the differences between the DSMs below this variation were
265 considered in the calculation of the detected sediment extraction. The detected extracted sediment volume
266 was then calculated for each experiment as follows:

267 $Vol_{detected} = \sum_p^1 (DSM_{before} - DSM_{after}) * res^2$, (4)

268 In Eq. (4), $Vol_{detected}$ is the volume of the extracted sediment as detected by the camera (cm³), p is the number
269 of pixels, DSM_{before} (cm) is the DSM calculated from the scan taken before the extraction, DSM_{after} (cm) is the
270 DSM calculated from the scan taken after the extraction, res (cm) is the resolution of the scan, which was 0.6
271 cm. To evaluate the camera's accuracy, the measured volume of the extracted sediment was compared to the
272 volume detected by the camera. The camera's accuracy was estimated between the detected volume and
273 measured volume as follows:

274 $MAE = \sum_1^n \frac{(Vol_{detected} - Vol_{measured})}{area}$. (5)

275 In Eq. (5), MAE (cm³/cm²) is the mean absolute error, n is the number of scans, $Vol_{measured}$ (cm³) is the volume
276 of the extracted sediment measured by the measuring cup, and the area is the total surface area monitored
277 by the camera (cm²).

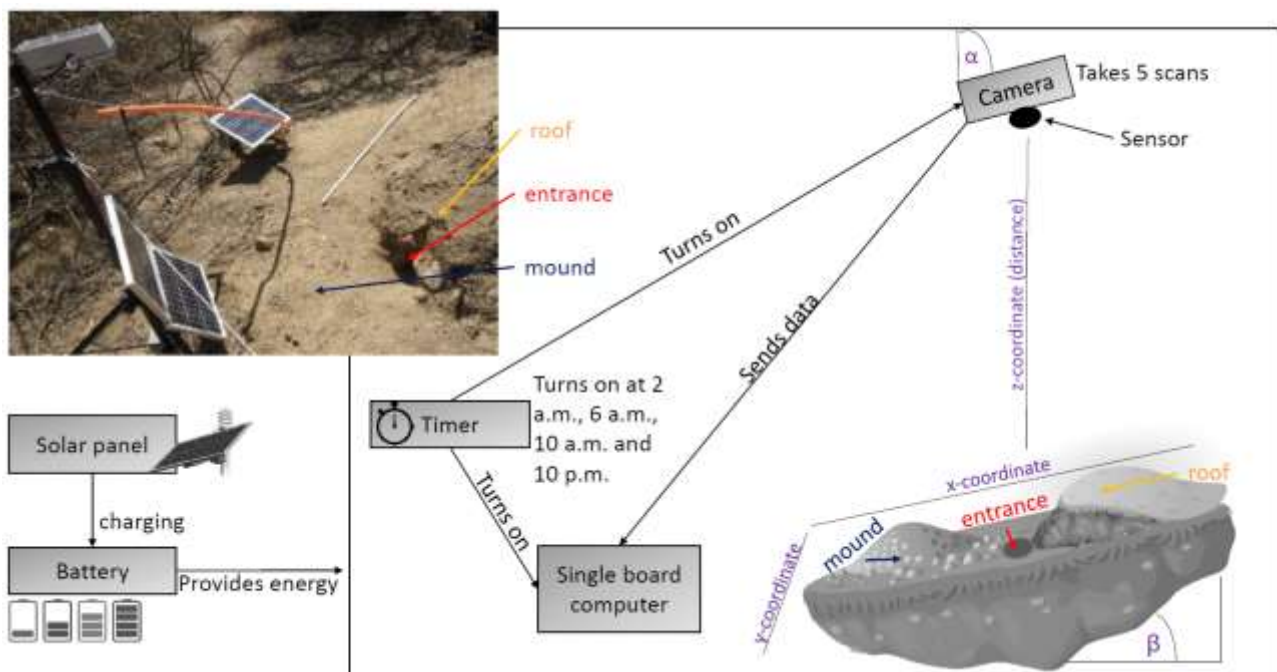
278

279 **3.4 Installation of the cameras in the field**

280 We installed 8 custom-tailored ToF-based cameras on 4 hillslopes in two climate zones in areas
281 including visible signs of bioturbation activity (burrows) and areas without visible signs of bioturbation (Fig. 3).
282 The cameras were installed in LC on the north-facing upper hillslope (LC-NU), north-facing lower hillslope (LC-
283 NL), south-facing upper hillslope (LC-SU) and the south-facing lower hillslope (LC-SL); in PdA on the north-
284 facing upper hillslope (PdA-NU), north-facing lower hillslope (PdA-NL), south-facing upper hillslope (PdA-SU)

285 and south-facing lower hillslope (PdA-SL). The custom-tailored cameras were installed during a field campaign
 286 in March 2019, the monitoring took place for seven months, and the data were collected in October 2019. The
 287 construction consisted of a 3D ToF-based sensor from Texas Instruments (Li, 2014), a RaspberryPi single board
 288 computer (SBC), a timer, a 12 V 12 Ah battery and three 20 W solar panels for unattended operation (Fig. 2).
 289 Solar panels were located at the camera pole and were recharging the battery via a charge controller. The
 290 camera was located approximately one meter above the surface, facing the surface with a tilt angle of 10
 291 degrees. The timer was set to close the electric circuit 4 times a day: at 1 a.m., 5 a.m., 8 a.m. and 10 p.m. At
 292 these times, the camera and the computer were turned on for 15 minutes. The camera turned on and took five
 293 scans delayed one second from each other and sent them to the SBC. Each camera had its own WiFi (Wireless
 294 Fidelity) and the data could be read from the SBC via Secure Shell (SSH). The cameras collected the data for
 295 the time period of 7 months.

296



297

298 **Figure 3.** Scheme and photo example of a Time-of-Flight-based camera installation in the field. The photo
 299 example is from upper north-facing hillslope in La Campana. Black boxes describe single installation parts.
 300 Purple descriptions are the variables needed for the correction of the scans. Roof, entrance and mound
 301 describe parts of the burrow. The x-, y- and z-coordinates are 3D coordinates identifying the position of each
 302 point in space, where the x-coordinate is the length, y-coordinate is the width and the z-coordinate is the
 303 distance between the camera sensor and the surface. α is the inclination of the camera, and β is the surface
 304 inclination.

305

306 3.5 Delineation of burrows and burrow embedding areas

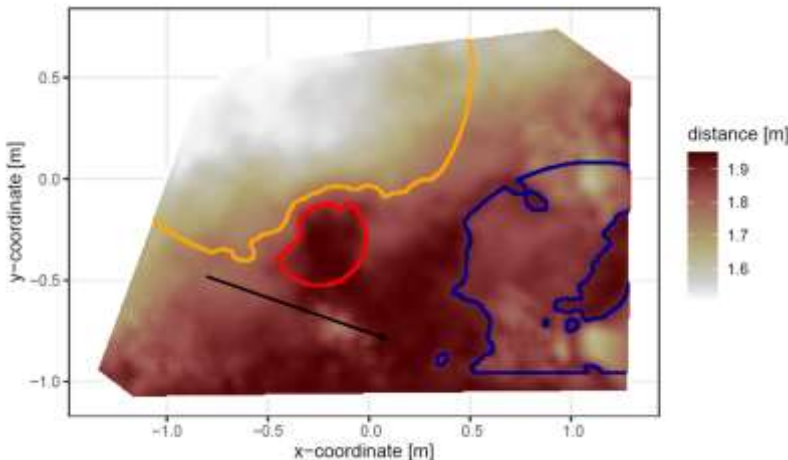
307 The surface area scanned by the cameras was divided by a delineation scheme into burrows (B) and
 308 burrow embedding areas (EM). The burrows included three sub-areas: (i) mound (M), (ii) entrance (E) and (iii)
 309 burrow roof (R). "Mound" describes the sediment excavated by the animal while digging the burrow. "Entrance"
 310 describes the entry to the animal burrow up to the depth possible to obtain via the camera. "Burrow roof"
 311 describes the part of the sediment above and uphill the burrow entrance (Bancroft et al. 2004). During the
 312 burrow's creation, sediment was not only excavated but also pushed aside and uphill the entrance, which

313 created the burrow roof. We assume that this elevated microtopographical feature then forms an obstacle for
314 sediment transported from uphill, which leads to its accumulation in this area. The remaining surface within
315 the camera's FOV was burrow embedding area. Please note, that this area may still be affected by the
316 burrowing activity of the animal and is not completely unaffected by the animal.

317 For the delineation, we used the DSM calculated from the point cloud, and a slope layer calculated
318 from the DSM (Horn 1981). The DSM had a size of 4 m^2 a resolution of 0.6 cm. Entrance was assigned to an
319 area determined by a search algorithm starting at the lowest point of the DSM (pixel with the highest z-
320 coordinate value). We increased the circular buffer around the starting point by one pixel until the average
321 depth of the new buffer points was not higher than the height of the camera above the surface, or until the
322 slope of at least 50% of the new buffer points was not 0. Then, we masked all pixels within the buffer with a
323 depth lower than the average depth of the points within the buffer, which had a slope that was 0. The remaining
324 pixels belonged to the entrance area. Then, the surface scan was divided into an uphill and downhill part with
325 regards to the entrance position. Both the uphill and the downhill parts were subdivided into 16 squares, so
326 that each of the four quadrants within the 2D grid (x- and y-axis) contained four squares. The squares had size
327 of 0.5 m^2 .

328 To delineate the mound in the downhill part, we first identified the highest points (pixel with the lowest z-
329 coordinate value) within all 16 squares. We then calculated the distance of these maxima to the entrance, and
330 the pixel located nearest to the entrance was identified as the highest point of the mound (i.e., seed point).
331 Consecutively, we increased the circular buffer around the seed point by one pixel until the average depth of
332 the new buffer points was not lower than the height of the camera above the surface, or until the slope of at
333 least 50% of the new buffer points was not 0. Then, we masked all pixels within the buffer with a depth higher
334 than the average depth of the points within the buffer, which had a slope that was 0. The remaining pixels were
335 classified as mound area. To delineate burrow roof, we used the same approach as for the delineation of
336 mound and applied it on the uphill part of the surface scan. We used the DEM and slope layers for the
337 delineation for several reasons. The distance from the surface to the camera was the most important parameter
338 to derive (i) the deepest point of the entrance and (ii) the highest point of the mound or burrow roof, as this
339 was (mostly) the closest point to the camera. After the angle correction of the z-coordinate according to chapter
340 3.2., the surface inclination of the areas without burrow was 0° , while the angle between the border of the
341 burrow entrance or mound and the burrow embedding surface was above 0° . Because neither the entrance
342 nor the mound have a perfect circular form, we would largely overestimate or underestimate the entrance or
343 mound size. Overestimate by not stopping the search algorithm until the angle between all new points of the
344 buffer to the rest of the buffer was 0° . Underestimate by stopping the algorithm when the angle of one point of
345 the buffer to the nearest point of the buffer was 0° . The value of 50% thus minimized the error. All pixels that
346 were not classified during the entire delineation process were treated as burrow embedding areas.

347 The position and the boundaries of entrance, mound and burrow roof were validated visually (Fig. 4 and A2).



348

349 **Figure 4.** Corrected digital surface model of the camera on the upper north-facing hillslope in La Campana
 350 with delineated areas. The point of origin of the coordinate system is at the camera nadir. Distance refers to
 351 the distance between surface and camera. The red line delineates the burrow entrance, blue the mound and
 352 orange the burrow roof. The area which was outside of any delineated area was classified as burrow
 353 embedding area. The arrow indicates a downhill direction of the hillslope.

354

355 In LC, the burrows always consisted of an entrance, mound and burrow roof. In PdA, there was no
 356 burrow roof on the upper hillslopes. Burrows without a burrow roof were located on shallower parts of the
 357 hillslopes (up to an inclination of 5°), and the angle of the burrow entrance to the ground was ~90°. Burrows
 358 with a burrow roof were located on steeper parts of the hillslopes (with an inclination above 5°), and the angle
 359 of the burrow entrance to the ground was ~45°.

360

361 **3.6 Calculation of animal-caused and rainfall-caused sediment redistribution**

362 We pairwise compared the DSMs of each scan with the scan saved before and identified 3 types of
 363 sediment redistribution which occurred in the time period between these images. The 3 types of redistribution
 364 were: a) animal caused; b) rainfall-caused; c) both animal and rainfall caused.

365 The animal-caused sediment redistribution occurred when the animal actively reworked sediment
 366 within its burrow. Following five prerequisites had to be met when the sediment redistribution was caused
 367 solely by the animal: (i) as the animal excavates sediment from the entrance, the depth of the entrance must
 368 increase in the second scan; (ii) as the excavated sediment accumulates on the mound, the height of the
 369 mound must increase in the second scan; (iii) as the burrowing might lead to an expansion or a collapse of the
 370 burrow roof, an increase or decrease of the burrow roof must occur between the scans; (iv) as the animal only
 371 digs within his burrow, no changes must occur between the two scans within the burrow embedding area by
 372 the animal; (v) no rainfall occurred during this period.

373 The rainfall-caused sediment redistribution was calculated as follows: From the data from the climate
 374 stations (Übernickel et al. 2021a), we calculated the daily precipitation in mm. The sediment redistribution
 375 recorded immediately and within five scans before and after a rainfall event is defined to be the result of the
 376 rainfall event. This was necessary as the climate stations are located up to a 15 km distance from the cameras
 377 (Fig. 1). To attribute sediment redistribution to rainfall event, three preconditions had to be met: (i) A rainfall
 378 event occurred; (ii) sediment is eroded from burrow roof, mound and the embedding area; (iii) sediment is
 379 accumulated within the burrow entrance.

380 To attribute sediment redistribution to a combination of animal activity and rainfall, four preconditions
381 had to be met: (i) A rainfall event occurred; (ii) sediment is eroded from embedding area; (iii) the height of
382 burrow roof and mound decreased or increased; (iv) the depth of burrow entrance increased.

383 The animal-caused sediment redistribution was calculated as the sediment volume excavated from
384 the entrance. Animal excavation always increased depth of the burrow entrance. The rainfall-caused sediment
385 redistribution was calculated as the sediment volume which eroded from the burrow roof and mound. During
386 a rainfall event, sediment eroding from burrow roof might accumulate within burrow entrances. In this case,
387 the depth of the burrow entrance decreased. No sediment could erode from the entrance during a rainfall
388 event. Decreased depth of a burrow entrance always points to sediment redistribution caused by rainfall,
389 increased depth of burrow entrance always means redistribution by animals. Rainfall-caused redistribution
390 always occurred before animal-caused redistribution, as without erosion caused by rainfall, the animals did not
391 need to reconstruct their burrows.

392

393 **3.7 Calculation of daily sediment mass balance budget**

394 The volume of the redistributed sediment was calculated daily and was then cumulated from the first
395 day of monitoring. For the calculation of the daily sediment redistribution, the change in the surface level
396 detected by the camera was calculated first. For each day, the scans from the day before and after the
397 respective day were averaged and subtracted. The average standard deviation of the z-coordinate of these
398 scans was 0.06 cm. As described in Section 2.2., all values with a difference below and above the threshold
399 value of 0.2 cm were set to 0. The redistributed sediment volume was then calculated from the surface change
400 for each pixel as follows:

401 $Vol_{redistributed} = (S_b - S_a) * res^2$ (6)

402 In Eq. (6), $Vol_{redistributed}$ ($cm^3 \text{ pixel}^{-1}$) is the volume of the calculated redistributed sediment, S_b (cm) the scan
403 before, S_a (cm) the scan after the rainfall event and res is the spatial resolution (cm). Using the daily volume
404 of the redistributed sediment per pixel, we calculated the daily mass balance budget by summing the volume
405 of sediment eroding or accumulating within each delineated area.

406

407 **3.8 Calculation of the overall volume of redistributed sediment after the period of 7 months**

408 From the camera data, we calculated the average cumulative volume of redistributed sediment for the
409 period of 7 months within burrows ($Vol_{burrows}$ ($cm^3 \text{ cm}^{-2} \text{ year}^{-1}$))) and burrow embedding ($Vol_{embedding}$ ($cm^3 \text{ cm}^{-2}$
410 year^{-1})) areas and the average sediment volume redistributed (excavated) by the animal (Vol_{exc} ($cm^3 \text{ cm}^{-2}$
411 year^{-1})), separately for each site. We estimated the volume of sediment that was redistributed during rainfall
412 events due to the presence of the burrow (Vol_{add} ($cm^3 \text{ cm}^{-2} \text{ year}^{-1}$))). Vol_{add} was calculated as the difference in
413 the redistributed sediment volume between burrows and burrow embedding areas according to Eq. (7).

414 $Vol_{add} = (Vol_{affected} - Vol_{unaffected}) * 1.71$, (7)

415 Additionally, we calculated the average volume of the redistributed sediment per burrow ($Vol_{per \text{ burrow}}$ [cm^3
416 $\text{burrow}^{-1} \text{ year}^{-1}$]).

417 $Vol_{per \text{ burrow}} = (Area_{burrow} * Vol) * 1.71$ (8)

418 In Eq. (8), $Area_{burrow}$ (cm^2) is the average size of the burrows that are monitored by the cameras; Vol is Vol_{burrow}
419 ($cm^3 \text{ cm}^{-2} \text{ year}^{-1}$), Vol_{exc} ($cm^3 \text{ cm}^{-2} \text{ year}^{-1}$) or Vol_{add} ($cm^3 \text{ cm}^{-2} \text{ year}^{-1}$).

420 We then upscaled the Vol_{burrow} ($cm^3 \text{ cm}^{-2} \text{ year}^{-1}$), Vol_{exc} ($cm^3 \text{ cm}^{-2} \text{ year}^{-1}$) and Vol_{add} ($cm^3 \text{ cm}^{-2} \text{ year}^{-1}$
421 $1)$) to the hillslope using the following approach. Hillslope-wide upscaling of the results generated in this study

422 was performed by using a previous estimation of vertebrate burrow density (Grigusova et al. 2021). In this
423 study, the density of burrows was measured in situ within eighty 100 m² plots and then upscaled to the same
424 hillslopes on which the cameras were located by applying machine-learning methods, using the UAV-data as
425 predictors. For upscaling, we applied a random forest model with recursive feature elimination. The model was
426 validated by a repeated Leave-One-Out cross validation. The density of vertebrate burrows was between 6
427 and 12 100 m⁻² in LC and between 0 and 12 100 m⁻² in Pan de Azúcar. Using the hillslope-wide predicted
428 vertebrate burrow densities (Dens_{burrow} (number of burrows 100 m⁻²)) from Grigusova et al. 2021, we estimated
429 the volume of redistributed sediment for each pixel of the raster layers (Vol_{per pixel} (cm³ m⁻² year⁻¹)) according
430 to Eq. (9):

431 $Vol_{per pixel} = Vol_{per burrow} * Dens_{burrow} * 1.71$ (9)

432 The average hillslope-wide volume of redistributed sediment (Vol_{hillslope-wide} (m³ ha⁻¹ year⁻¹)) was then
433 estimated as follows:

434 $Vol_{hillslope-wide} = \sum_1^m Vol_{per pixel} * 0.001 * 1.71$, (10)

435 In Eq (10), m is the number of pixels.

436

437 4. Results

438 4.1 Camera accuracy and data availability

439 The accuracy between the measured extracted sediment volume and sediment volume calculated
440 from the camera scans was very high (MAE = 0.023 cm³ cm⁻², R² = 0.77, SD = 0.02 cm³ cm⁻², Fig. A3). The
441 accuracy between the calculated and measured extracted sediment was higher when the two scans taken
442 before as well as after the extraction of the sediment were averaged and the sediment volume was estimated
443 using these averaged scans. When calculating the redistributed sediment from solely one scan before and
444 after extraction, the accuracy slightly decreased (MAE = 0.081 cm³ cm⁻², R² = 0.64). The cameras tended to
445 overestimate the volume of redistributed sediment. Six out of eight custom-tailored cameras collected data
446 over the seven-month period (Table A2). One camera collected data for a period of three months and one
447 camera stopped working a few days after installation. The quantity of usable point clouds taken at 1 a.m., 5
448 a.m. and 10 p.m. was higher than of point clouds taken at 8 a.m. Approximately 20% of points was removed
449 from the point clouds before final analysis due to the high scattering at the point cloud corners. After data
450 filtering (see Section 3.2.), 1326 scans were usable and for 86% of the days, at least one usable scan was
451 available. The usable scans were distributed continuously within the monitoring period.

452

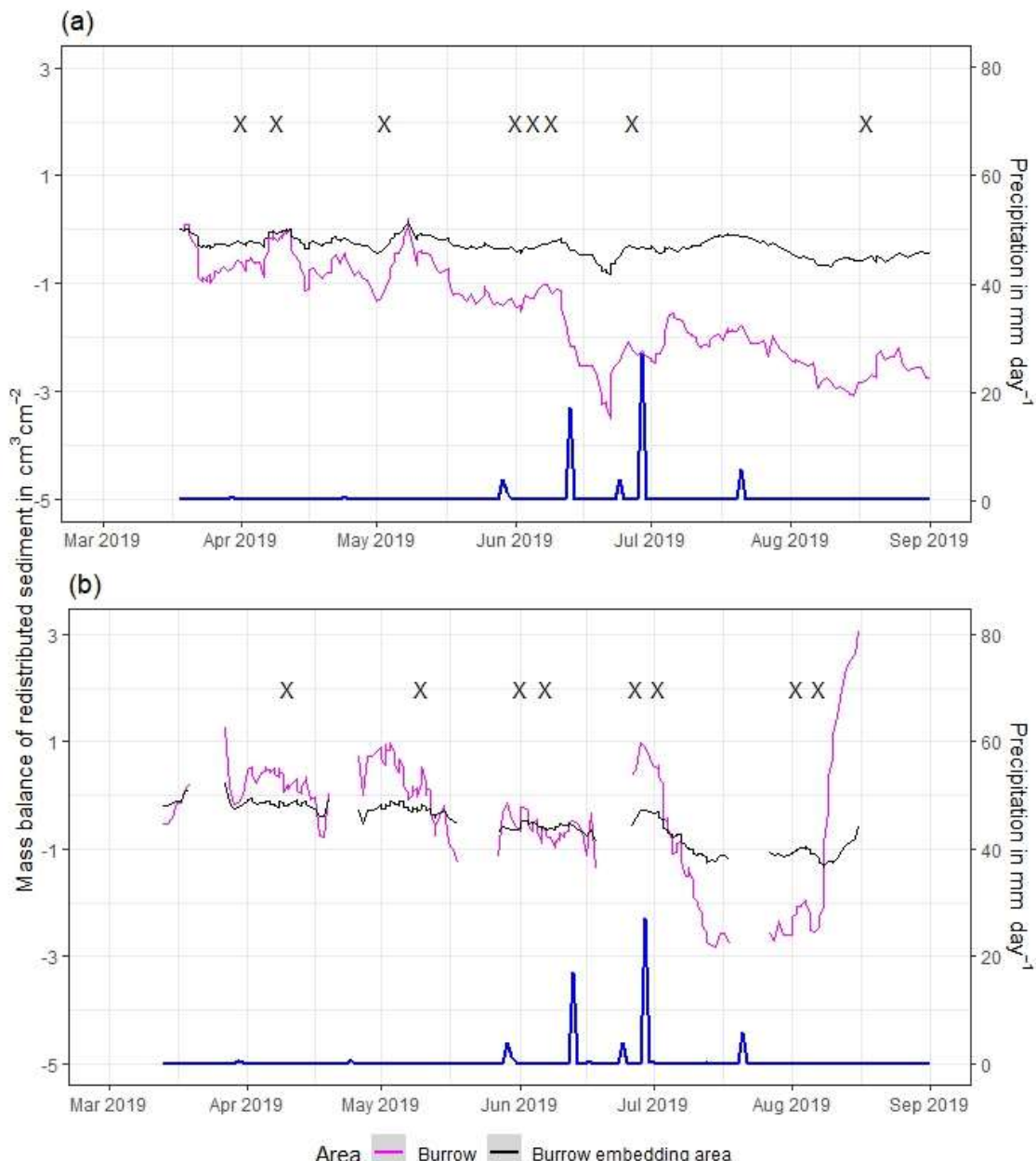
453 4.3 Mass balance of redistributed sediment

454 The cameras detected (i) sediment redistribution directly following rainfall events and (ii) due to the
455 burrowing activity in times without rainfall (Fig. 5, A4 and A5). In all cases, burrows (entrance, burrow roof and
456 mound) exhibited higher sediment redistribution rates than burrow embedding areas. In addition, the volume
457 of redistributed sediment by animal activity was higher after a rainfall event occurred.

458 In the following, the dynamics are exemplary explained for four cameras. Animal burrowing activity
459 was detected seven times by the camera LC NU (Fig. 5a, A4, A5) during the monitoring period, by an increase
460 in sediment volume in the area delineated as mound. Simultaneously, the burrow entrance showed signs of
461 modification and sediment accumulation, but these changes were less clear. Overall, the volume of the
462 excavated soil varied. From April until June, up to 0.5 cm³ cm⁻² of sediment was excavated by the animal and
463 accumulated on the mound. From June until September, animal burrowing activity was detected at four time

464 slots (5 June 2019, 9 June 2019, 1 July 2019 and 18 August 2019) and sediment volume of up to $2 \text{ cm}^3 \text{ cm}^{-2}$
465 accumulated each time on the mound, burrow roof and within the entrance. During the rainfall events of up to
466 20 mm day^{-1} on 16 June 2019, 27 mm day^{-1} on 29 June 2019 and 7 mm day^{-1} on 13 July 2019, sediment
467 volume of up to $4 \text{ cm}^3 \text{ cm}^{-2}$ eroded, especially from the burrow roof and the mound while a sediment volume
468 of up to $1 \text{ cm}^3 \text{ cm}^{-2}$ accumulated within the entrance during each rainfall event. Camera LC-SL (Fig. A4, A5)
469 showed burrowing activities eight times and sediment volumes of up to $3 \text{ cm}^3 \text{ cm}^{-2}$ accumulated within the
470 entrance and burrow roof. The camera detected sediment erosion of up to $2 \text{ cm}^3 \text{ cm}^{-2}$ after a rainfall event of
471 27 mm day^{-1} on 27 July 2019. On the south-upper hillslope, the camera detected animal burrowing activity six
472 times, with a sediment accumulation of up to $3 \text{ cm}^3 \text{ cm}^{-2}$ (Fig. A2 and A3).

473 In contrast, camera PdA-NU pointed to animal burrowing activity up to 15 times where up to $1 \text{ cm}^3 \text{ cm}^{-2}$
474 of sediment volume was redistributed from the entrance to the mound (Fig. 5b, A4, A5). At the end of June
475 on 27 June 2019, a rainfall event of 1.5 mm day^{-1} occurred and up to $2 \text{ cm}^3 \text{ cm}^{-2}$ of sediment eroded from the
476 burrow roof and accumulated within the burrow entrance. We observed increased sediment redistribution by
477 the animal after the rainfall events. Camera PdA-SL evenly revealed animal burrowing activity up to 15 times
478 ((Fig. A4, A5)). The burrowing had a strong effect on the sediment redistribution. The rainfall event of 1.5 mm
479 day^{-1} on 27 June 2019 did not cause any detectable surface change.



480
481

482 **Figure 5.** Examples of the mass balance of redistributed sediment for burrows and burrow embedding areas
483 (a) The record of the camera on the upper north-facing hillslope in La Campana showed that larger rainfall
484 events cause a negative sediment balance (sediment loss), followed by a phase of positive sediment mass
485 balance after approximately 3 days due to sediment excavation; (b) The record of the camera on the upper north-facing
486 hillslope in Pan de Azúcar hillslope showed a similar pattern to the camera on the upper north-facing
487 hillslope, but the phase of positive mass balance was delayed in comparison. The blue line is the daily
488 precipitation in mm day^{-1} , and "X" marks the days at which animal burrowing activity was detected. Positive
489 values indicate sediment accumulation. Negative values indicate sediment erosion. Mass balances for all
490 cameras are displayed in Fig. A2 and A3.

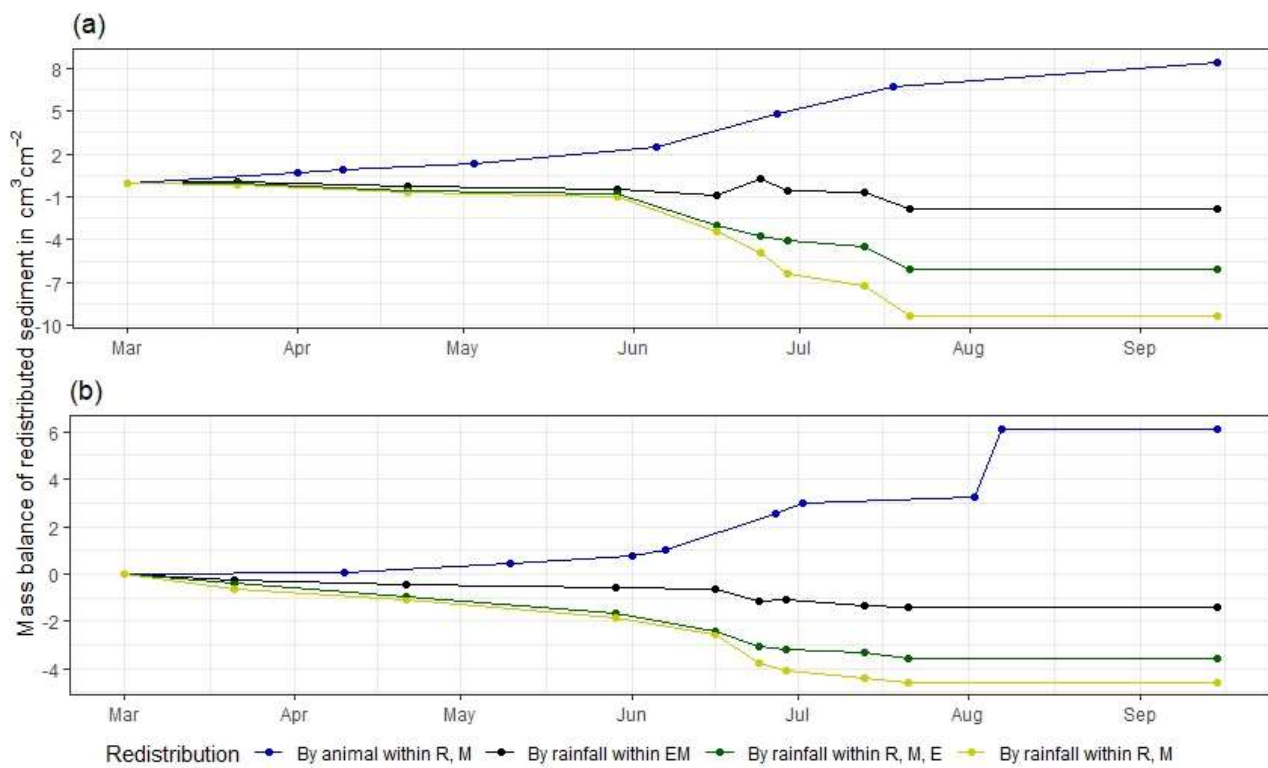
491

492 The analysis of cumulative volume of the redistributed sediment caused by burrowing animal activity
493 and rainfall over the monitored period of seven months for all eight cameras showed a heterogeneous pattern.

494 In LC, the cumulative volume of the sediment excavated by the animal within the burrow roof and
 495 mound increased continuously (Fig. 6, A7). Especially between the rainfall events from June until August, a
 496 cumulative volume of on average $6.5 \text{ cm}^3 \text{ cm}^{-2}$ was excavated by the animal. We calculated that, on average,
 497 $8.53 \text{ cm}^3 \text{ cm}^{-2}$ cumulatively eroded from the burrow roof and mound; while $2.44 \text{ cm}^3 \text{ cm}^{-2}$ sediment volume
 498 accumulated within the entrance (Fig. 6, A7). These results indicate that 28% of sediment eroding from the
 499 burrow roof accumulated within the entrance, while over 62% of sediment eroded downhill. Averaged over all
 500 camera scans, 338% more sediment was redistributed by rain within burrow compared to the burrow
 501 embedding area (Fig. 7).

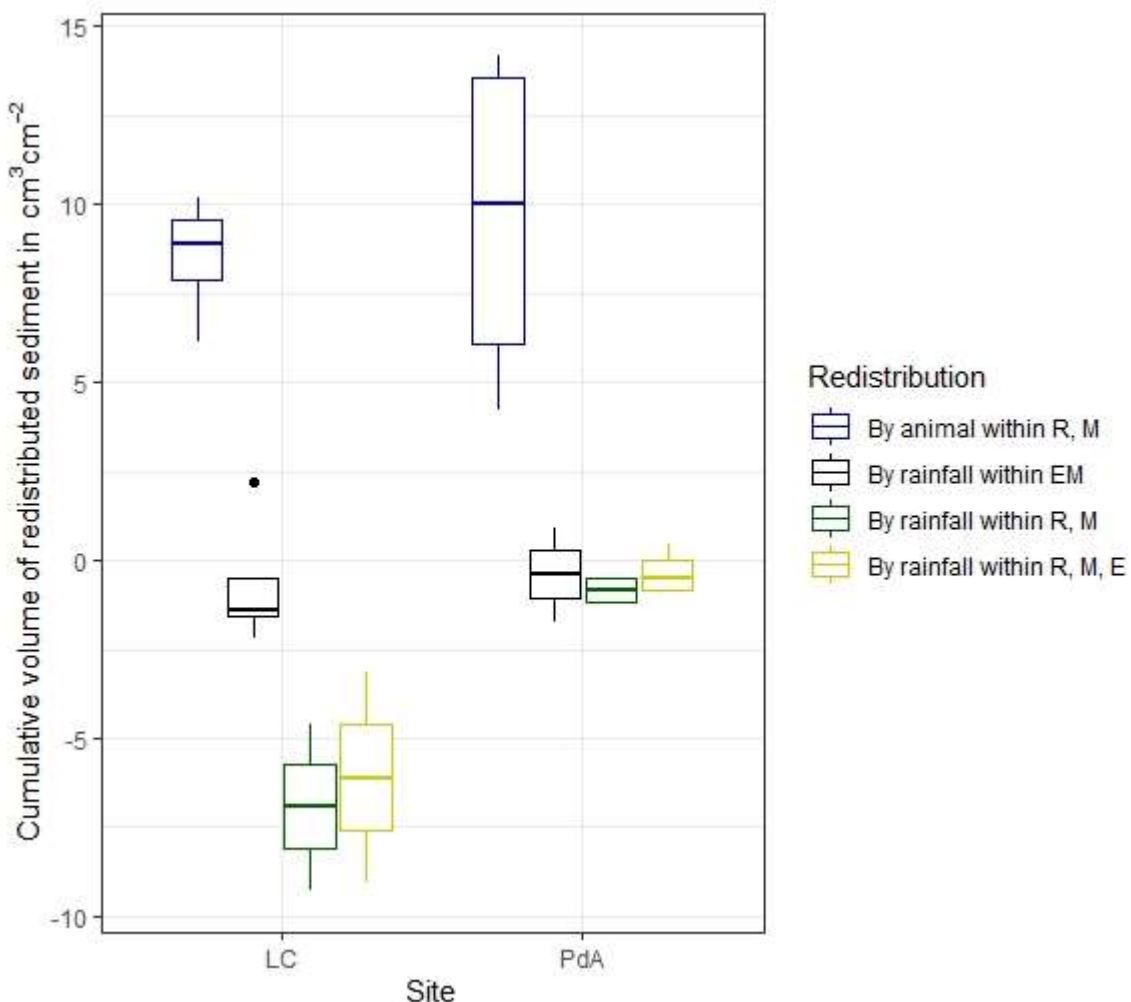
502 In PdA, cameras continuously detected animal burrowing activity and excavation of the sediment (Fig.
 503 A7). The volume of the detected excavated sediment increased steadily within all cameras. The cumulative
 504 sediment accumulation surpasses the sediment eroded due to the rainfall. The volume of the sediment eroded
 505 within the burrows was 40% higher than within the burrow embedding areas. The results show that
 506 approximately 50% of the eroded sediment accumulated within the entrance (Fig. 7).

507



508

509 **Figure 6.** Examples of the cumulative volume of redistributed sediment within burrows and burrow embedding
 510 areas caused by animal burrowing activity or rainfall in mediterranean La Campana: (a) Upper north-facing
 511 hillslope; (b) Lower south-facing hillslope. Positive values indicate sediment accumulation. Negative values
 512 indicate sediment erosion. E is the burrow entrance; M is the mound; R is burrow roof; EM is the burrow
 513 embedding area. Cumulative volumes for all cameras are in Fig. A7.



514

515 **Figure 7.** Cumulative volume of the redistributed sediment for the time period of 7 months for all cameras.
 516 Positive values indicate sediment accumulation. Negative values indicate sediment erosion. Whiskers indicate
 517 the median of sediment redistribution. E is the burrow entrance; M the mound; R is the burrow roof; EM is
 518 burrow embedding area; LC stands for National Park La Campana in the mediterranean climate zone; PdA
 519 stands for National Park PdA in the arid climate zone.

520

521 **4.4 Volume of redistributed sediment**

522 The average size of the burrows was 84.3 cm^2 ($\text{SD} = 32.5 \text{ cm}^2$) in LC and 91.3 cm^2 in PdA ($\text{SD} = 8.5 \text{ cm}^2$).
 523 The animals burrowed on average $1.2 \text{ times month}^{-1}$ in LC and $2.3 \text{ times month}^{-1}$ in PdA. The volume of the
 524 excavated sediment was $102.2 \text{ cm}^3 \text{ month}^{-1}$ in LC and $124.8 \text{ cm}^3 \text{ month}^{-1}$ in PdA. Each time the animals
 525 burrowed, they excavated 42 cm^3 sediment volume in LC and 14.3 cm^3 sediment volume in PdA. The
 526 burrowing intensity increased in winter after the rainfall occurrences in LC and stayed constant during the
 527 whole monitoring period in PdA. The burrows deteriorate after rainfall events with a rate of $73.0 \text{ cm}^3 \text{ month}^{-1}$ or
 528 $63.9 \text{ cm}^3 \text{ event}^{-1}$ in LC and $10.5 \text{ cm}^3 \text{ month}$ or $24.5 \text{ cm}^3 \text{ event}^{-1}$.

529 The overall volume of the sediment excavated by the animal and redistributed during rainfall events
 530 varied between the sites (Table 1). The volume of the sediment redistributed by the animal was lower in LC
 531 than in PdA. However, on the hillslope scale, a higher total area-wide volume of excavation was calculated for
 532 LC compared to PdA, due to the higher burrow density in LC. The volume of the sediment redistributed within

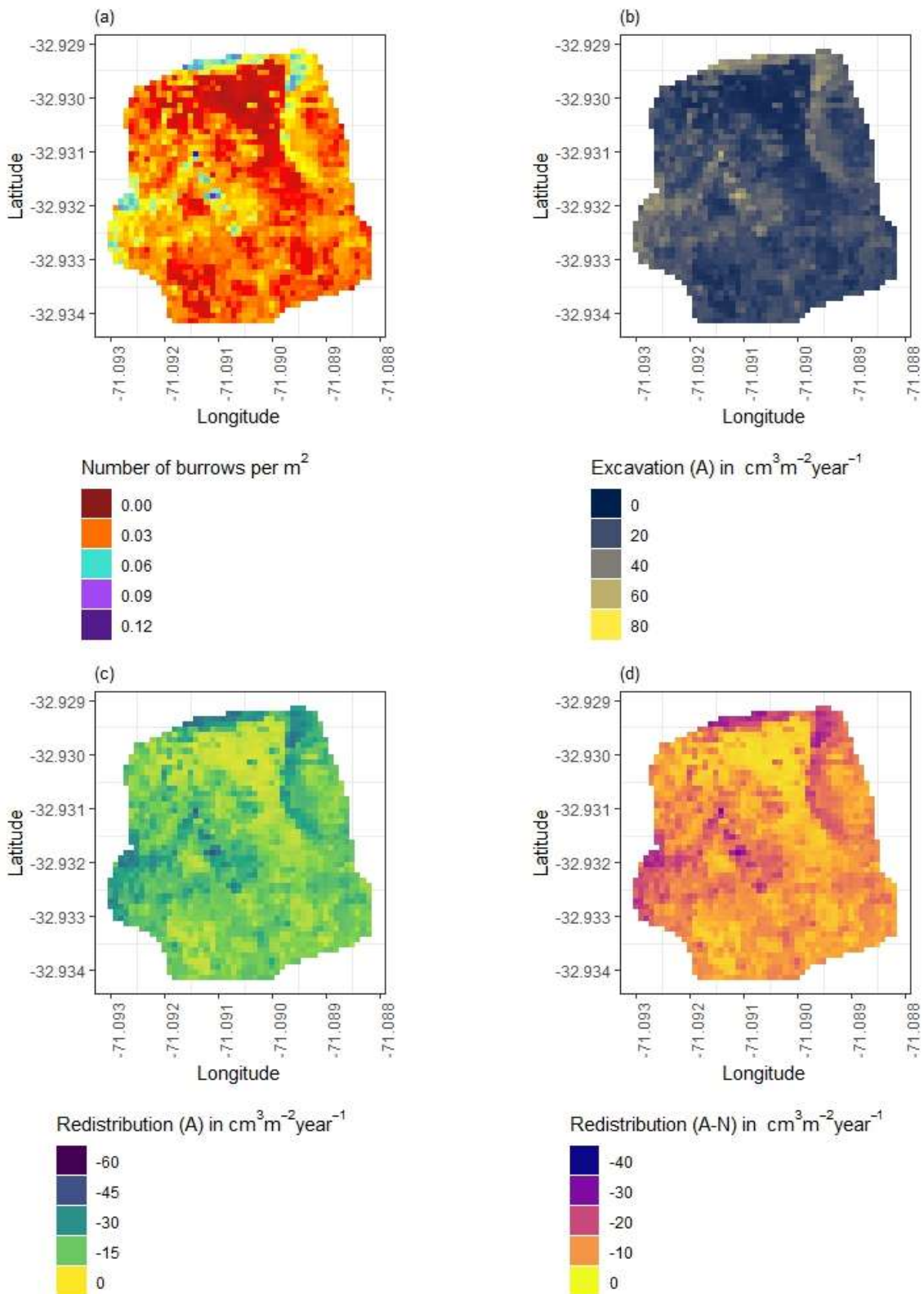
533 burrows during rainfall events was higher in LC than in PdA. The volume of additionally redistributed sediment
534 due to the presence of burrows was higher in LC than in PdA (Table 2, Fig. 8).

535

536 **Table 2.** Summary of the volume of redistributed sediment, according to area and disturbance type. Vol_{exc}
537 describes volume of the sediment excavated by the animals. $\text{Vol}_{\text{burrow}}$ describes volume of the sediment
538 redistributed during rainfall events within burrows. Vol_{add} describes the difference in redistributed sediment
539 volume within burrows and burrow embedding areas during rainfall. Positive values indicate sediment
540 accumulation; negative values indicate sediment erosion.

Disturbance	Area	PdA	LC
Vol_{exc}	Burrow	$16.4 \text{ cm}^3 \text{ cm}^{-2} \text{ year}^{-1}$	$14.6 \text{ cm}^3 \text{ cm}^{-2} \text{ year}^{-1}$
	Per burrow	$1498.6 \text{ cm}^3 \text{ burrow}^{-1} \text{ year}^{-1}$	$1226.1 \text{ cm}^3 \text{ burrow}^{-1} \text{ year}^{-1}$
	Hillslope-wide	$0.8 \text{ m}^3 \text{ ha}^{-1} \text{ year}^{-1}$	$0.7 \text{ m}^3 \text{ ha}^{-1} \text{ year}^{-1}$
$\text{Vol}_{\text{affected}}$	Burrow	$-1.9 \text{ cm}^3 \text{ cm}^{-2} \text{ year}^{-1}$	$-10.4 \text{ cm}^3 \text{ cm}^{-2} \text{ year}^{-1}$
	Per burrow	$-126.3 \text{ cm}^3 \text{ burrow}^{-1} \text{ year}^{-1}$	$-876.8 \text{ cm}^3 \text{ burrow}^{-1} \text{ year}^{-1}$
	Hillslope-wide	$-0.1 \text{ m}^3 \text{ ha}^{-1} \text{ year}^{-1}$	$-0.4 \text{ m}^3 \text{ ha}^{-1} \text{ year}^{-1}$
Vol_{add}	Burrow	$-1.1 \text{ cm}^3 \text{ cm}^{-2} \text{ year}^{-1}$	$-7.3 \text{ cm}^3 \text{ cm}^{-2} \text{ year}^{-1}$
	Per burrow	$-48.3 \text{ cm}^3 \text{ burrow}^{-1} \text{ year}^{-1}$	$-619.2 \text{ cm}^3 \text{ burrow}^{-1} \text{ year}^{-1}$
	Hillslope-wide	$-0.1 \text{ m}^3 \text{ ha}^{-1} \text{ year}^{-1}$	$-0.3 \text{ m}^3 \text{ ha}^{-1} \text{ year}^{-1}$

541



542

543 **Figure 8.** Example of the hillslope-wide volume of redistributed sediment on the south-facing hillslope in La
 544 Campana: (a) Density of burrows as estimated by Grigusova et al. (2021); (b) Volume of the sediment
 545 excavated by the animals; (c) Volume of the sediment redistributed during rainfall events within burrows; (d)
 546 Volume of additionally redistributed sediment during rainfall events due to the presence of the burrows. The
 547 values were calculated per burrow as stated in Section 3.7. by subtracting the sediment volume redistributed
 548 within burrows from the sediment volume redistributed within burrow embedding area and then upscaled. The
 549 letters in brackets indicate if the upscaling was conducted using data from burrows or burrow embedding areas.

550 “B” stands for burrow. By “EM-B”, the redistribution calculated within burrow embedding areas was subtracted
551 from the redistribution calculated within burrows to obtain the additional volume of redistributed sediment due
552 to the burrows’ presence. Positive values indicate sediment accumulation. Negative values indicate sediment
553 erosion.

554

555

556 **5. Discussion**

557 Our results showed that the custom-made ToF device is a suitable tool for high-resolution, automated
558 monitoring of surface changes, applicable also in remote areas. The continuous observation of sediment
559 redistribution over a longer time period provided new insights into the relative importance of burrowing animals
560 for hillslope sediment flux. Our research revealed that the presence of vertebrate burrows increases hillslope
561 sediment redistribution rates much more than previously assumed (increase of up to 208%). We showed that
562 the quantity of animal-related sediment redistribution, however, varied with rainfall occurrence, with an increase
563 in sediment redistribution between 40% in the arid research area and 338% percent in the mediterranean
564 research area.

565

566 **5.1 Suitability of the ToF - cameras for surface monitoring**

567 The newly introduced monitoring technique ToF enables an automatic monitoring of surface changes
568 on a microtopographic scale, and is less costly and invasive than other techniques. The measurement
569 continuity of the device also allows for the analysis of ongoing biogeomorphological processes in high temporal
570 and spatial resolution.

571 With regard to the costs, measurement frequency and sampling autonomy, the custom-made ToF device
572 constitutes an improvement to earlier studies which used laser scanning technology to monitor
573 microtopographic changes (Table A5). This is because previous studies applied expensive laser scanning for
574 the estimation of sediment redistribution, and due to the costs of the instrument it was not left in the field for
575 continuous measurements, and hence research sites had to be revisited for each measurement
576 (Nasermoaddeli und Pasche 2008; Eltner et al. 2016a; Eltner et al. 2016b; Hänsel et al. 2016). The estimated
577 costs in studies using time-lapse photogrammetry were similar to our study (up to 5000 USD) (James und
578 Robson 2014; Galland et al. 2016; Mallalieu et al. 2017; Eltner et al. 2017; Kromer et al. 2019; Blanch et al.
579 2021). However, time-lapse monitoring needs several devices set up in different viewing angles, which
580 increases installation efforts and disturbance significantly.

581 In terms of data quality, our ToF device is more precise or comparable to those employed in earlier
582 studies using ToF. The accuracy of the camera ($R^2 = 0.77$) was in the range of previous studies ($R^2 = 0.26$ –
583 0.83 (Eitel et al. 2011), Table A5). The horizontal point spacing of our cameras was 0.32 cm, and the maximum
584 number of points per cm^2 was 8.5. These values are similar to previous studies in which the used devices had
585 a horizontal point spacing in the range of 0.25–0.57 cm (Kaiser et al. 2014; Nasermoaddeli und Pasche 2008))
586 (Table A5), and the maximum number of points per cm^2 in a range of 1 point–25 points cm^{-2} (Eitel et al. 2011;
587 Longoni et al. 2016) (Table A5).

588 Our cameras tended to slightly overestimate or underestimate the volume of redistributed sediment.
589 This error occurs when the pulse reflects from several vertical objects such as walls or, in our case, branches
590 or stones and then enters the camera sensor. This phenomenon was also observed in previous studies
591 applying laser scanners and is inevitable if the goal is to study surface changes under natural field conditions

592 (Kukko und Hyppä 2009; Ashcroft et al. 2014). During operation of the cameras, we learnt that our newly
593 developed instruments are particularly capable of delivering usable scans at night. This is likely due to the
594 strong scattered sunlight reaching the camera sensor during the day, blurring the data (Li 2014). Thus, in future
595 studies, we recommend focusing on nocturnal operation to prevent light contamination.

596

597 **5.2 The role of climate variability and burrowing cycles**

598 We have found that rainfall plays a key role in triggering burrowing activity, which means that wet
599 seasons experience higher sediment redistribution rates than dry seasons. In the year of investigation (2019),
600 the dry season lasted from January until April, and from September until December (8 months), and the wet
601 season lasted from May until August (4 months). The monitoring period lasted from March until October which
602 covered 3 dry and 4 wet months (7 months in total). A yearly rate of sediment redistribution can be calculated
603 by simply averaging the redistribution rate of the 7 monitored months and multiplying this result by 12 months,
604 which results in an average redistribution rate of $0.4 \text{ m}^2 \text{ ha}^{-1} \text{ year}^{-1}$ for LC and $0.1 \text{ m}^2 \text{ ha}^{-1} \text{ year}^{-1}$ for PdA.
605 However, because burrowing activity and rain-driven sediment redistribution is mainly determined by rainfall,
606 this method might have led to an overestimation of the annual redistribution rate based on averaging, because
607 the unmonitored part of the year 2019 was predominantly dry (Übernickel et al. 2021a). This can be accounted
608 for by adding five times the dry month redistribution rate to the monitored 7 months, which leads to a lower
609 annual redistribution rates for LC of $0.3 \text{ m}^2 \text{ ha}^{-1} \text{ year}^{-1}$ and for PdA of $0.1 \text{ m}^2 \text{ ha}^{-1} \text{ year}^{-1}$. This difference between
610 both values ($0.1 \text{ m}^2 \text{ ha}^{-1} \text{ year}^{-1}$ for LC and under $0.1 \text{ m}^2 \text{ ha}^{-1} \text{ year}^{-1}$ for PdA) can be interpreted as the uncertainty
611 range for the year of observation. However, decadal rainfall variability indicates that the year of monitoring
612 (2019) was among the drier years of the last 30 years (Yáñez et al. 2001) which means our results might
613 underestimate sediment redistribution on a longer time perspective.

614 Furthermore, the phenology of the burrowing animals is an additional source for uncertainty when
615 calculating annual rates. The most common burrowing animal families in the area are active from March until
616 October (refer to section earlier), and hence their burrowing activity is fully covered during the monitoring
617 period. None of the most common burrowing animal families were reported to be active from November until
618 February. This is also in line with our observations, because burrowing intensity increased from March until
619 May, reached its peak between May and June and declined until September (Figure 6). By extrapolating from
620 7 months to one-year period, our estimated excavation was $0.7 \text{ m}^2 \text{ ha}^{-1} \text{ year}^{-1}$ in LC and $0.8 \text{ m}^2 \text{ ha}^{-1} \text{ year}^{-1}$ in
621 PdA. By adding five times the low active months to the 7 months of observation, the estimated excavation
622 would be $0.6 \text{ m}^2 \text{ ha}^{-1} \text{ year}^{-1}$ in LC and $0.6 \text{ m}^2 \text{ ha}^{-1} \text{ year}^{-1}$ in PdA. The excavation uncertainty range is thus 0.1
623 $\text{m}^2 \text{ ha}^{-1} \text{ year}^{-1}$ for LC and $0.2 \text{ m}^2 \text{ ha}^{-1} \text{ year}^{-1}$ for PdA. In summary, the discussion on the uncertainties of
624 extrapolating single or sub-annual observations to annual rates clearly underpins the importance of high
625 resolution, longer-term monitoring, which can be warranted with the here developed technology.

626

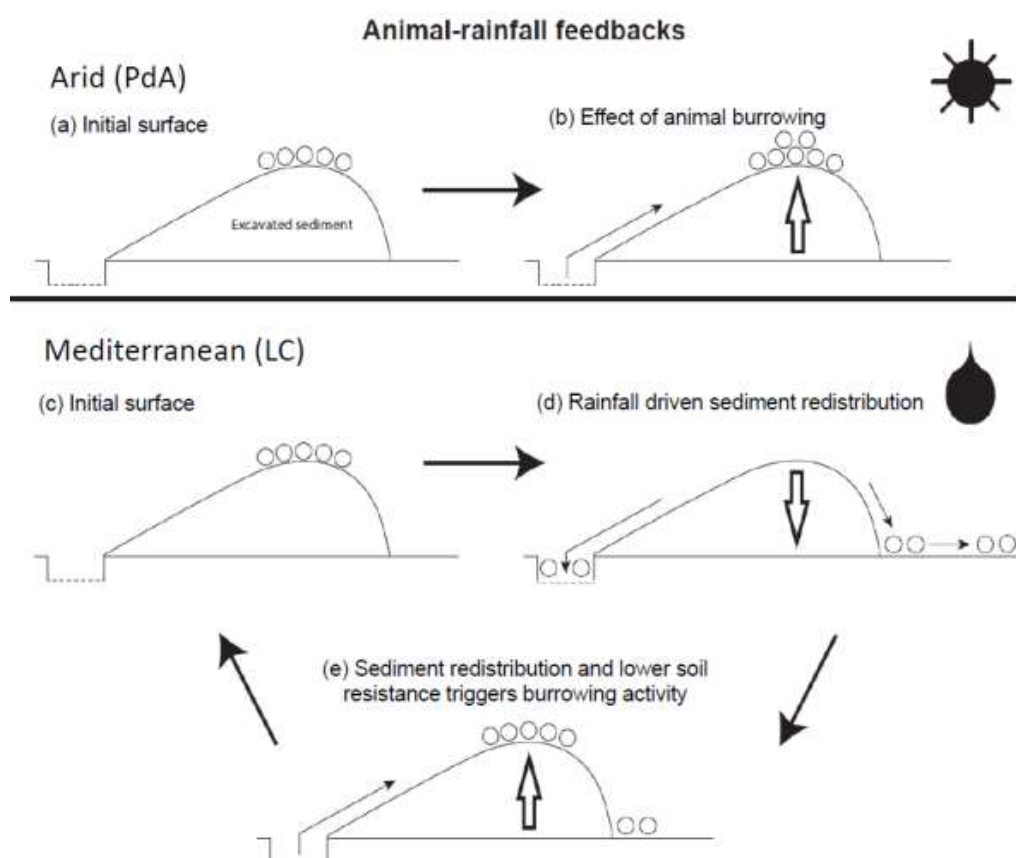
627

628 **5.3. Sediment Redistribution**

629 Our research reveals that the presence of vertebrate burrows generally increases hillslope sediment
630 redistribution. We show, however, that the ratio between the sediment redistribution caused by rainfall within
631 burrow and burrow embedding areas varies between climate zones. Sediment redistribution within burrow
632 areas was 40% higher at the arid research site, and at the mediterranean research site, it was 338% higher
633 when compared to burrow embedding area (Table A6).

634 By monitoring microtopographical changes in a high spatio-temporal resolution, we found that the
 635 occurrence of larger rainfall events played a two-fold, accelerating role in influencing sediment redistribution
 636 (Fig. 9). Firstly, rainfall-runoff eroded burrow material caused increased sediment loss. This was followed by
 637 animal burrowing activity after the rainfall. This means that rainfall triggered animal burrowing activity which
 638 was very likely related to a lower burrowing resistance of the soil due to the increased soil moisture (Rutin
 639 1996; Romañach et al. 2005; Herbst und Bennett 2006). This double feedback led to frequently occurring but
 640 small redistribution rates. However, cumulatively, the mechanism increased downhill sediment fluxes. Previous
 641 studies most likely missed this low magnitude but frequent surface processes due to a lower monitoring
 642 duration and frequency, or artificial laboratory conditions, and thus, did not quantify the full volume of
 643 redistributed sediment associated with burrowing activity. To quantify all occurred sediment redistribution
 644 processes, a continuous surface monitoring, like the here presented, is needed.

645



646

647 **Figure 9.** Scheme of animal-driven and rainfall-driven sediment redistribution processes in both investigated
 648 climate zones: (a) Describes the initial surface of the burrow before the start of a sediment redistribution
 649 process, and (b) the animal excavation process in the arid climate zone. Here, due to rarely occurring rainfall
 650 events, sediment redistribution is mostly controlled by the animal burrowing activity; (c) describes the initial
 651 burrow surface in the mediterranean climate zone, (d) the process of sediment redistribution during a rainfall
 652 event and (e) the subsequent animal burrowing activity. Burrowing is triggered by decreased soil resistance
 653 due to the increased soil moisture after rainfall as well as by sediment accumulation within the burrow's
 654 entrance. Burrowing activity leads to a new supply of sediment being excavated to the surface. In the
 655 mediterranean climate zone, sediment redistribution is controlled by both animal burrowing activity and rainfall.
 656 The alternating excavation and erosion process ultimately lead to an increase in redistribution rates.

657

658 Our results indicate an up to 338% increase in the sediment volume redistributed during rainfall events
659 measured within burrows when compared to burrow embedding areas. In contrast to our result, the maximum
660 increase estimated in previous studies was 208% (Table A6, (Imeson und Kwaad 1976). The two climate
661 zones also show different patterns: In the mediterranean climate, the contribution of animals' (vertebrates')
662 burrowing activity appear larger than previously observed by using field methods such as erosion pins or
663 splash traps (from –3% until – 208%, Table A6, (Imeson und Kwaad 1976; Hazelhoff et al. 1981; Black und
664 Montgomery 1991). In contrast, in arid PdA, our study found a much smaller increase (40%, Table A6) in the
665 sediment volume redistributed during rainfall events measured within burrows when compared to burrow
666 embedding areas. This is lower than previously estimated (125%, Table A6, (Black und Montgomery 1991)).
667 However, solely one rainfall event above 0.2 mm day⁻¹ occurred during our monitoring period. Hence, we
668 conclude that the contribution of burrowing activity of animals to hillslope sediment transport is much larger in
669 areas with frequent rainfall events than previously thought, while it has been realistically estimated by previous
670 studies for areas with rare rainfall events (Table A6).

671 Magnitudes of sediment volume redistributed within burrows similar to our results were previously
672 obtained solely in studies applying rainfall simulators. These studies estimated an increase in the volume of
673 sediment redistributed during rainfall events, measured within burrows when compared to burrow embedding
674 areas, to be between 205% and 473% (Table A6, (Li et al. 2018; Chen et al. 2021). However, a rainfall simulator
675 can only provide data on surface processes within a plot of a few m² in size and under ideal laboratory
676 conditions while ignoring the uphill microtopography, vegetation cover and distribution (Iserloh et al. 2013),
677 which were shown to reduce erosion rates. More importantly, the rainfall intensity on hillslopes decreases with
678 (i) the angle of incidence of the rain, (ii) the inclination of the surface and iii) the relative orientation of the
679 sloping surface to the rain vector (Sharon 1980). When simulating a rainfall event with the same rainfall volume
680 as in the field, the rain is induced directly over the treated surface and has thus a higher velocity which leads
681 to an increased splash erosion than under natural conditions (Iserloh et al. 2013). We thus propose that the
682 rainfall experiments overestimate the erosion rate while the correct erosion rate can be measured solely under
683 field conditions.

684 Cumulative sediment redistribution within burrow roof, mound and entrance was, on average, 28%
685 lower than cumulative sediment redistribution only within the mound and the burrow roof (Figure A7). These
686 results suggest that 28% of the eroded sediment from animal mounds and burrow roofs is re-accumulated
687 within the burrow entrance during rainfall-runoff events, and the remaining 62% is incorporated into overall
688 hillslope sediment flux. Our numbers contrast with previous studies, which quantified that about 58% of the
689 sediment excavated by animals will accumulate back in the burrow entrance and only 42% is incorporated to
690 downhill sediment flux (Andersen 1987; Reichman und Seabloom 2002). Hence, our results indicate not only
691 higher redistribution rates within burrows by burrowing animals but also point to much higher supply of
692 sediment to the downhill sediment flux than previously thought.

693 Our cost-effective ToF device provides data on surface changes in a high spatio-temporal resolution.
694 The high temporal resolution was able to unravel ongoing low magnitude but frequent animal excavation and
695 erosion processes. The high spatial resolution enabled us to estimate the exact volume of sediment fluxes
696 from the burrows downhill. The here presented results indicate that the contribution of burrowing animals on
697 the burrow as well as on the hillslope scale was much higher than previously assumed. Our results can be
698 integrated into long-term soil erosion models that rely on soil processes and improve their accuracy by
699 including animal-induced surface processes on microtopographical scales in their algorithms.

700	
701	
702	Funding: This study was funded by the German Research Foundation, DFG [grant numbers
703	BE1780/52-1, LA3521/1-1, FA 925/12-1, BR 1293-18-1], and is part of the DFG Priority Programme
704	SPP 1803: EarthShape: Earth Surface Shaping by Biota, sub-project “Effects of bioturbation on rates
705	of vertical and horizontal sediment and nutrient fluxes”.
706	Institutional Review Board Statement: Not applicable.
707	Informed Consent Statement: Not applicable.
708	Acknowledgments: We thank CONAF for the kind support provided during our field campaign.
709	Competing interests: There is no conflict of interest.
710	Author contribution: JB, AL and SA planned the campaign; PG and SA performed the measurements; PG
711	analysed the data and wrote the manuscript draft; AL, JB, NF, RB, KÜ, LP, CR, DK and PP reviewed and edited
712	the manuscript.
713	Code/Data availability: Code and all raw data can be provided by the corresponding author upon request.
714	
715	Appendices
716	Table A1. List of abbreviations
	α [°] Tilt angle of the camera
	b [°] Surface inclination
	Ω Threshold value for the scan scattering error
	B Burrow
	Area_{burrow} mean in the field measured size of the burrows which are monitored
	Area total surface area monitored by the camera
	BD Bulk density
	c [m/s] Speed of light
	D Distance from the camera to the object
	Dens_{burrow} Burrow density
	DSM Digital surface model
	DSM_{after} DSM calculated from the scan taken after the extraction
	DSM_{before} DSM calculated from the scan taken before the extraction
	EM Burrow embedding area
	Entrance entrance to the animal burrow
	g [-] ratio [-] of the reflected photons to all photons
	LC National Park LC
	LC-NL Camera in LC on the lower north-facing hillslope
	LC-NU Camera in LC on the upper north-facing hillslope
	LC-SL Camera in LC on the lower south-facing hillslope
	LC-SU Camera in LC on the upper south-facing hillslope
	MAE Mean absolute error
	MAP [°] Mean annual precipitation
	m.a.s.l. Meters above sea level

MAT	Mean annual temperature
mClay [%]	Mean content of clay
mean_{z-coordinate}	Mean value of the z-coordinates
Mound	the sediment excavated by the animal while digging the burrow
mSand [%]	Mean content of sand
mSilt [%]	Mean content of silt
n	Number of scans
PdA	National Park Pan de Azúcar
PdA-NL	Camera in PdA on the lower north-facing hillslope
PdA-NU	Camera in PdA on the upper north-facing hillslope
PdA-SL	Camera in PdA on the lower south-facing hillslope
PdA-SU	Camera in PdA on the upper south-facing hillslope
Res	Resolution
Roof	sediment pushed aside and uphill the entrance during burrow creation
S_a	scan after the rainfall event
S_b	scan before the rainfall event
SBC	Single board computer
sd_{z-coordinate}	standard deviation of the z-coordinates
SSH	Secure shell
t [s]	Overall time of camera illumination
TOC [%]	Total organic carbon
ToF	Time-of-Flight
Vol_{burrow}	volume of redistributed sediment within burrow
Vol_{detected}	volume of the extracted sediment as detected by the camera
Vol_{add}	difference in redistributed sediment volume between burrows and burrow embedding areas
Vol_{exc}	Volume of the sediment excavated by the animal
Vol_{hillslope-wide}	Hillslope-wide volume of redistributed sediment
Vol_{measured}	volume of the extracted sediment measured by the measuring cup
Vol_{per burrow}	Volume of redistributed sediment per burrow
Vol_{per pixel}	Volume of redistributed sediment per pixel
Vol_{redistributed}	volume of the calculated redistributed sediment
Vol_{embedding}	volume of redistributed sediment within burrow embedding area
y_i	distance of the point to the point of origin at the camera nadir
z_{cor}	Corrected z-coordinate
z_{uncor}	Uncorrected z-coordinate

717

718 **Table A2.** Number of usable scans for each camera

Camera	Latitude	Longitud e	Number of scans	Percentage of usable scans taken at 1am / 5am / 8am / 10pm	Time period
---------------	-----------------	-------------------	------------------------	---	--------------------

PdA-NU	-25.98131	-70.6166	238	29 / 27 / 20 / 24	18.3.-18.9.
PdA-NL	-25.98277	-70.61278	52	24 / 0 / 40 / 36	27.3.-31.5
PdA-SU	-25.97477	-70.61641	351	30 / 26 / 32 / 11	16.3.-19.9.
PdA-SL	-25.97177	-70.61409	167	48 / 38 / 7 / 8	16.3.-19.9.
LC-NU	-32.95230	-71.06231	215	37 / 20 / 8 / 33	9.3.-9.9.
LC-NL	-32.93928	-71.08613	3	-	6.3.-12.9
LC-SU	-32.93078	-71.09066	160	22 / 28 / 26 / 25	28.3.-22.5
LC-SL	-32.93110	-71.08987	167	27 / 25 / 22 / 26	16.3.-19.9.

719

720 **Table A3.** Summary of the volume of redistributed sediment, according to area and disturbance type. Vol_{exc}
 721 describes volume of the sediment excavated by the animals. $\text{Vol}_{\text{burrow}}$ describes volume of the sediment
 722 redistributed during rainfall events within burrows. Vol_{add} describes the difference in redistributed sediment
 723 volume within burrows and burrow embedding area during rainfall.

Disturbance	Area	PdA	LC
Vol_{exc}	Burrow	16.41 cm ³ cm ⁻² year ⁻¹	14.62 cm ³ cm ⁻² year ⁻¹
	Per burrow	1498.66 cm ³ burrow ⁻¹ year ⁻¹	1226.61 cm ³ burrow ⁻¹ year ⁻¹
	Hillslope-wide	0.18 m ³ ha ⁻¹ year ⁻¹	0.67 m ³ ha ⁻¹ year ⁻¹
Vol_{burrow}	Burrow	-1.97 cm ³ cm ⁻² year ⁻¹	-10.44 cm ³ cm ⁻² year ⁻¹
	Per burrow	-126.36 cm ³ burrow ⁻¹ year ⁻¹	-876.38 cm ³ burrow ⁻¹ year ⁻¹
	Hillslope-wide	-0.05 m ³ ha ⁻¹ year ⁻¹	-0.48 m ³ ha ⁻¹ year ⁻¹
Vol_{add}	Burrow	-1.18 cm ³ cm ⁻² year ⁻¹	-7.37 cm ³ cm ⁻² year ⁻¹
	Per burrow	-48.36 cm ³ burrow ⁻¹ year ⁻¹	-619.2 cm ³ burrow ⁻¹ year ⁻¹
	Hillslope-wide	-0.02 m ³ ha ⁻¹ year ⁻¹	-0.34 m ³ ha ⁻¹ year ⁻¹

724

725

726 **Table A4.** Summary of the volume of redistributed sediment, according to area and disturbance type. Vol_{exc}
 727 describes volume of the sediment excavated by the animals. $\text{Vol}_{\text{burrow}}$ describes volume of the sediment
 728 redistributed during rainfall events within burrows. Vol_{add} describes the difference in redistributed sediment
 729 volume within burrows and burrow embedding areas during rainfall.

Disturbance	Area	PdA	LC
Vol_{exc}	Burrow	9.57 cm ³ cm ⁻² 7 months ⁻¹	8.53 cm ³ cm ⁻² 7 months ⁻¹
	Per burrow	874.22 cm ³ burrow ⁻¹ 7 months ⁻¹	715.52 cm ³ burrow ⁻¹ 7 months ⁻¹
	Hillslope-wide	0.11 m ³ ha ⁻¹ 7 months ⁻¹	0.39 m ³ ha ⁻¹ 7 months ⁻¹
Vol_{burrow}	Burrow	-1.15 cm ³ cm ⁻² 7 months ⁻¹	-6.09 cm ³ cm ⁻² 7 months ⁻¹
	Per burrow	-73.71 cm ³ burrow ⁻¹ 7 months ⁻¹	-511.22 cm ³ burrow ⁻¹ 7 months ⁻¹
	Hillslope-wide	-0.03 m ³ ha ⁻¹ 7 months ⁻¹	-0.28 m ³ ha ⁻¹ 7 months ⁻¹

Vol_{add}	Burrow	-0.69 cm ³ cm ⁻² 7 months ⁻¹	-4.30 cm ³ cm ⁻² 7 months ⁻¹
	Per burrow	-28.21 cm ³ burrow ⁻¹ 7 months ⁻¹	-361.20 cm ³ burrow ⁻¹ 7 months ⁻¹
	Hillslope-wide	-0.01 m ³ ha ⁻¹ 7 months ⁻¹	-0.2 m ³ ha ⁻¹ 7 months ⁻¹

730

731 **Table A5.** Review of studies which used laser scanners for the estimation of surface processes.

Reference	R ²	Error	Horizontal point spacing	Points per cm ⁻²	Model	Price
Our results	0.77	0.15 cm	0.32 cm	8.5	Texas Instruments OPT3101	900 USD
(Eitel et al. 2011)	0.23-0.86	0.07 cm	NA	25	Leica ScanStation 2	102 375 USD
(Eltner et al. 2013)	NA	0.4 cm	NA	6.4	Riegl LMS-Z420i	16 795 USD
(Kaiser et al. 2014)	NA	NA	0.57 cm	NA	Riegl LMS-Z420i	16 795 USD
(Longoni et al. 2016)	NA	NA	NA	1	Riegl LMS-Z420i	16 795 USD
(Morris et al. 2011)	NA	0.5 cm	NA	NA	Maptek I-Site 4400LR	240 000 USD
(Nasermoaddeli und Pasche 2008)	NA	0.2 cm	0.25 cm	NA	Leica CyraX HDS 2500	4500 USD
(Thomsen et al. 2015)	NA	NA	0.4 cm	NA	Leica ScanStation 2	102 375 USD

732

733 **Table A6.** Review of studies which estimated the sediment redistribution within burrows and burrow embedding 734 areas and the proposed impact.

Reference	Climate	Animals	Method	Monitoring period	Frequenc	Burrows	Burrow embeddi	impa
					y		ng area	ct
(Imeson und Kwaad 1976)	continental	Rodents	erosion pins	15 months	monthly	20 mm		NA
(Imeson und Kwaad 1976)	continental	Rodents	splash boards	15 months	monthly	91.75g 24.49 cm ⁻²	94g = 3.75 cm ³	-3%

(Imeson und 1976)	continental	Rodents	rainfall simulation	One-time measurement	NA	0.2 g	–	0.009 g	–	+208 %
						0.73 g		0.23 g		
				on (7.5 cm / hour)						
				intensity)						
(Imeson 1977)	continental	Vertebra	rainfall simulation	One-time measurement	NA	0.18-0.3	0.146	+123		
						100 J ⁻¹ m ⁻²	100 J ⁻¹ m			
				on nt		rain				
(Hazelhoff et al. 1981)	continental	Earthworms	splash traps	12 months	monthly	NA	NA	+180		
(Black und Montgome ry 1991)	arid	pocket gopher	erosion pins	10 months	2 months	NA	NA	+125		
(Hakonson 1999)	temperate	pocket gophers	rainfall simulation	2 years	2 weeks	2.4 – 8.7	4.4 – 15	-43%		
				2 years (60 mm / hour)		mg ha ⁻¹	mg ha ⁻¹			
(Li et al. 2018)	temperate	mole crickets	rainfall simulation	One time (36 mm / hour)	15 measurements	22.1 g cm ⁻²	115 cm ⁻²	5 g cm ⁻²	123 cm ⁻²	+473 %
						5.2 cm ⁻²	1.09 cm ³			
(Li et al. 2018)	temperate	mole crickets	rainfall simulation	One time (36 mm / hour)	15 measurements	35.3 g cm ⁻²	5 g cm ⁻²	123 cm ⁻²		+473 %
						220.5 cm ⁻²	cm ⁻²			
						= 6.24 cm ³	1.09 cm ³			
(Chen et al. 2021)	laboratory	chinese zocor	rainfall simulation	One-time measurement	3 measurements	2,69 g cm ⁻²	0,88 cm ⁻²	g cm ⁻²	–	+205 %
						= 2.69 cm ³	0.88 cm ³			

735

736

737 **Table A7.** Review of studies which estimated the sediment redistribution within burrows, average burrow
738 density as found in the literature and area-wide yearly contribution of burrowing animals to sediment
739 redistribution.

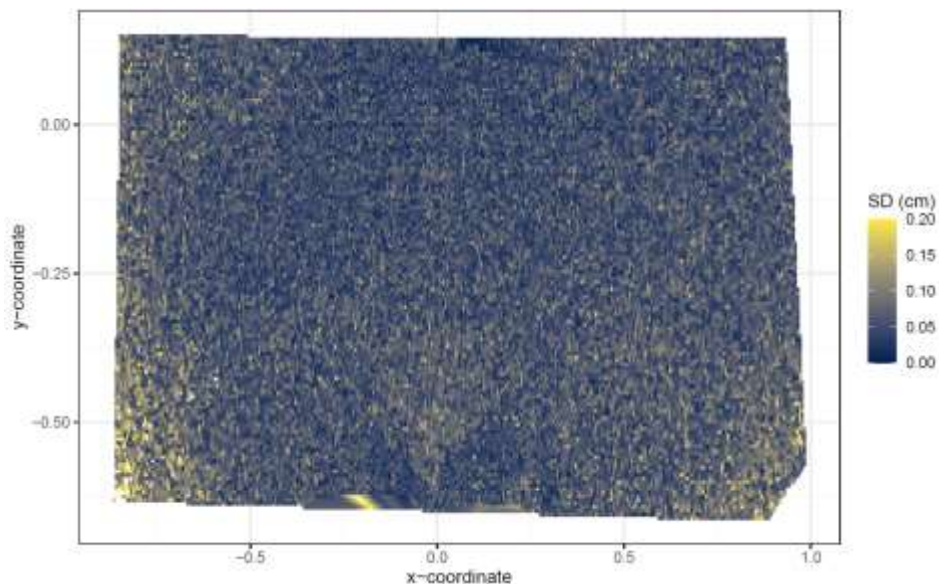
Climate	Animals	Burrows		Average burrow density	Average burrow size	Area-wide redistribution		
Continental	Rodents	91.75g	24.49	14 625 m ⁻² = cm ⁻² = 3.75 cm ³ cm ⁻² (Imeson und Guo 2017) und Kwaad (1976)	24.49	cm ²	0.183 m ³	ha ⁻¹ year ⁻¹
Temperate	mole crickets	22.1 g	115 cm ⁻² = 5.2 cm ³ cm ⁻² (Li et al. 2018)	405 ha ⁻¹	115 cm ² (Li et al. 2018) Fowler 1984)	(Li et al. 2018)	0.24 m ³	ha ⁻¹ year ⁻¹
Temperate	mole crickets	35.3 g	220.5 cm ⁻² cm ⁻² = 6.24 cm ³ cm ⁻² (Li et al. 2018)	405 ha ⁻¹	220.5 cm ² (Li et al. 2018) Fowler 1984)	(Li et al. 2018)	0.56 m ³	ha ⁻¹ year ⁻¹
Lab	chinese zocor	2,69 g cm ⁻² = 2.69 cm ³ cm ⁻² = (Chen et al. 2021)	94.69 2500m ⁻² 0.04 m ⁻² = 400 ha ⁻¹	1256 cm ²			1.35 m ³	ha ⁻¹ year ⁻¹

740

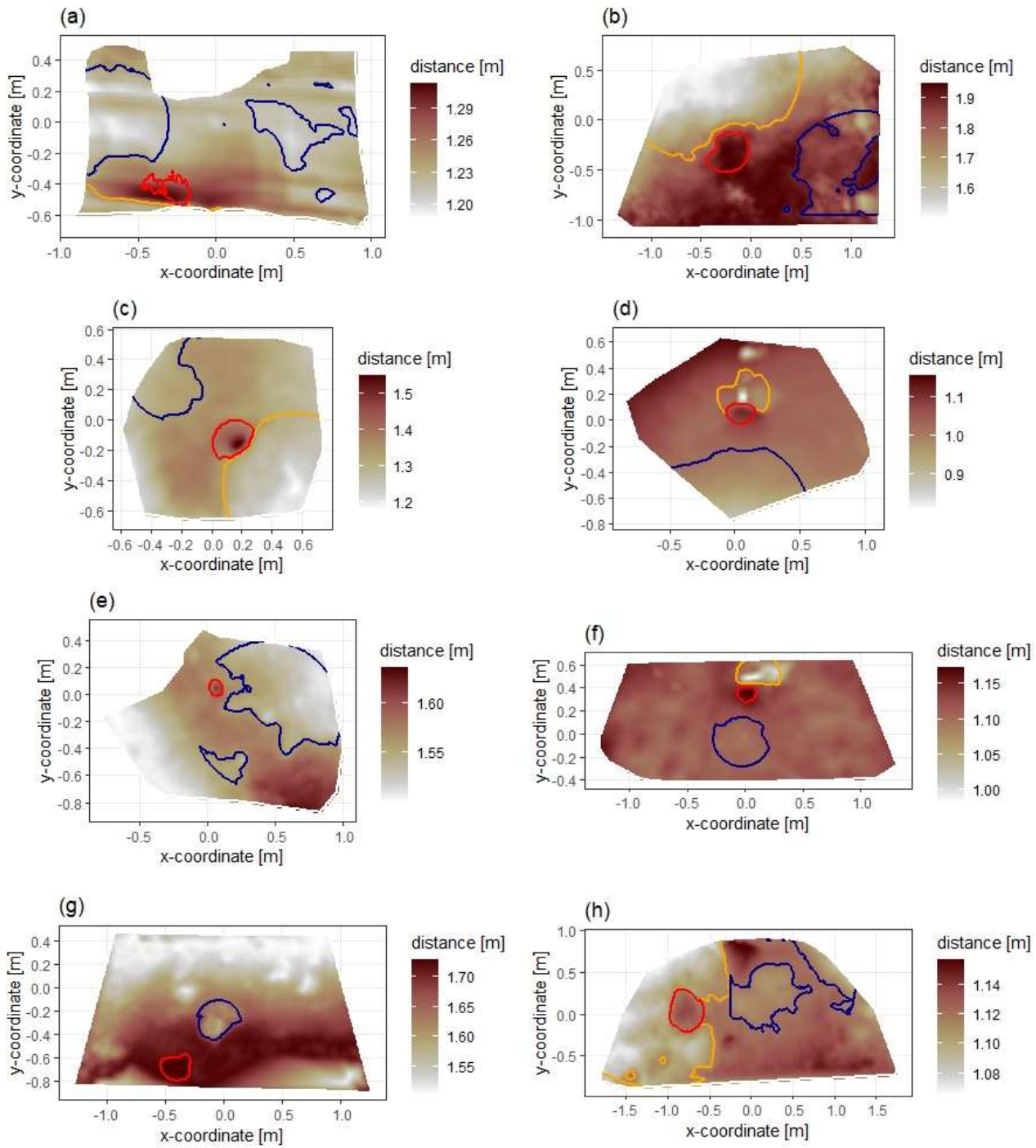
741 **Table A8.** Review of studies which estimated the volume of sediment excavated by burrowing animals.

Climate	Animals	Method	Monitoring period	Frequency	volume of the excavated sediment		
(Black und Arid 1991)	porcupines	mound volume	3 years	yearly	0.2 m ³	ha ⁻¹ year ⁻¹	
(Black und Arid 1991)	isopods	mound volume	3 years	yearly	0.11 m ³	ha ⁻¹ year ⁻¹	
(Black und Arid 1991)	pocket gopher	mound volume	2 years	3 model runs	0.05 – 0.11 m ³ ha ⁻¹ year ⁻¹		
(Rutin 1996)	Subtropical	scorpions	mound volume	6 months	2-29 days	0.42 m ³ ha ⁻¹ year ⁻¹	
(Hall et al. 1999)	Alpine	rodents	mound volume	1 year	yearly	0.02 m ³ ha ⁻¹ year ⁻¹	
(Hall et al. 1999)	Alpine	bears	mound volume	1 year	yearly	0.49 m ³ ha ⁻¹ year ⁻¹	
(Yoo et al. 2005)	Arid	pocket gopher	mound volume	1 year	One model run	0.1-0.2 m ³ ha ⁻¹ year ⁻¹	

742
743

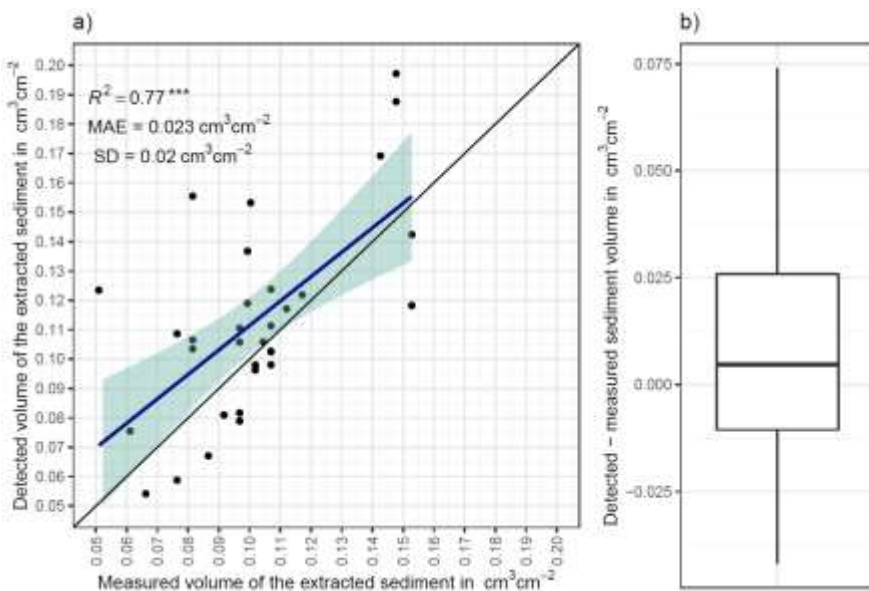


744
745 **Figure A1.** Standard deviation of the z-coordinate of unprocessed five scans showed exemplary for the camera
746 on the upper north-facing hillside. SD is standard deviation. The error increases with distance from the camera
747 nadir point. The standard deviation was here calculated from scans before any corrections.
748
749

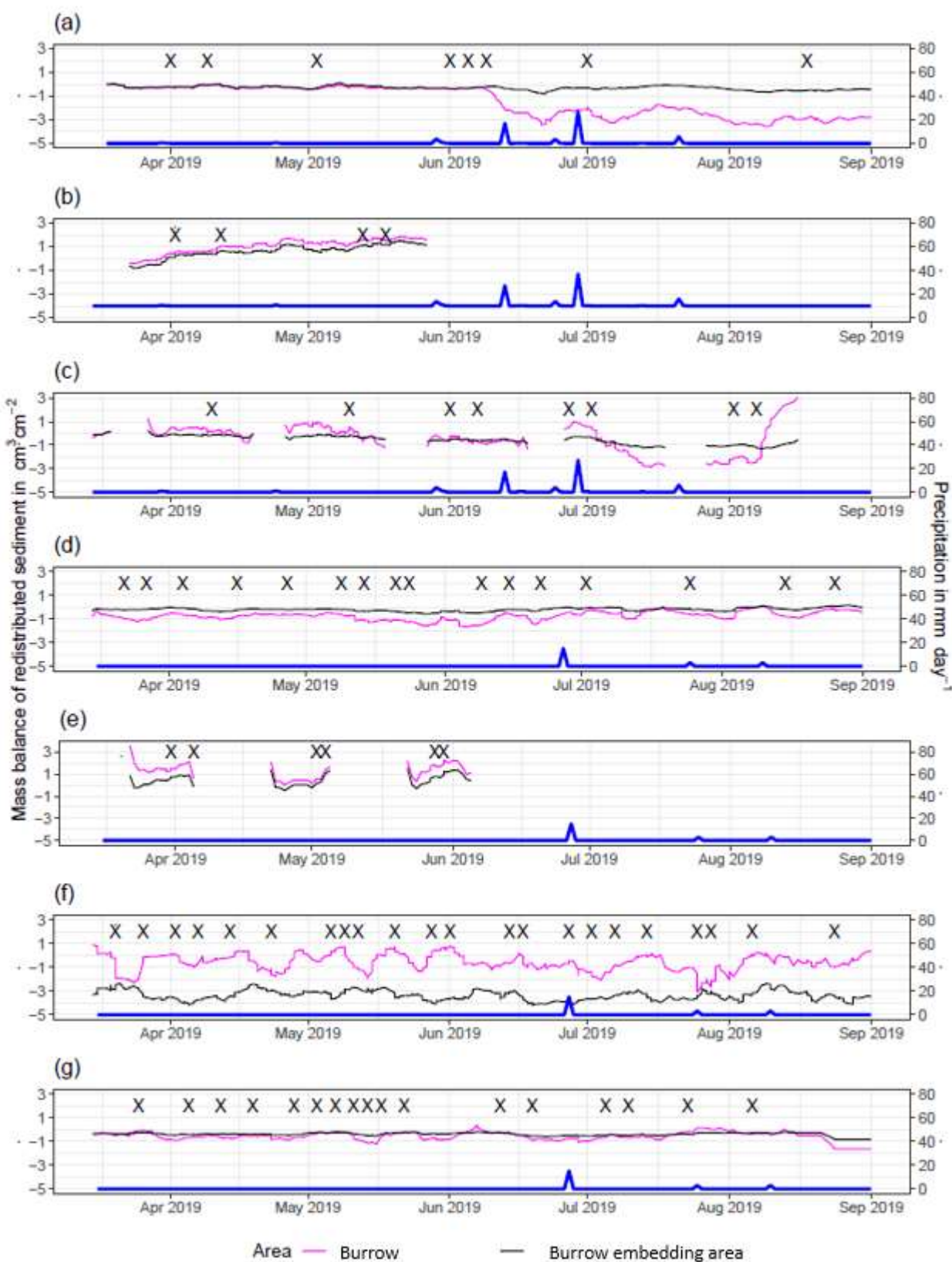


750

751 **Figure A2.** Delineation of the areas. The point of origin of the coordinate system is at the camera nadir. Depth
 752 is the distance between the surface and the camera. Red is the outline of the burrow entrance. Green is the
 753 outline of mound. Orange is the outline of burrow roof. Area which is not outlined is burrow embedding area.
 754 Arrow indicates downhill direction of the hillslope. (a) LC-NU. (b) LC-NL (c) LC-SU. (d) LC-SL. (e) PdA-NU. (f)
 755 PdA-NL. (g) PdA-SU. (h) PdA-SL.

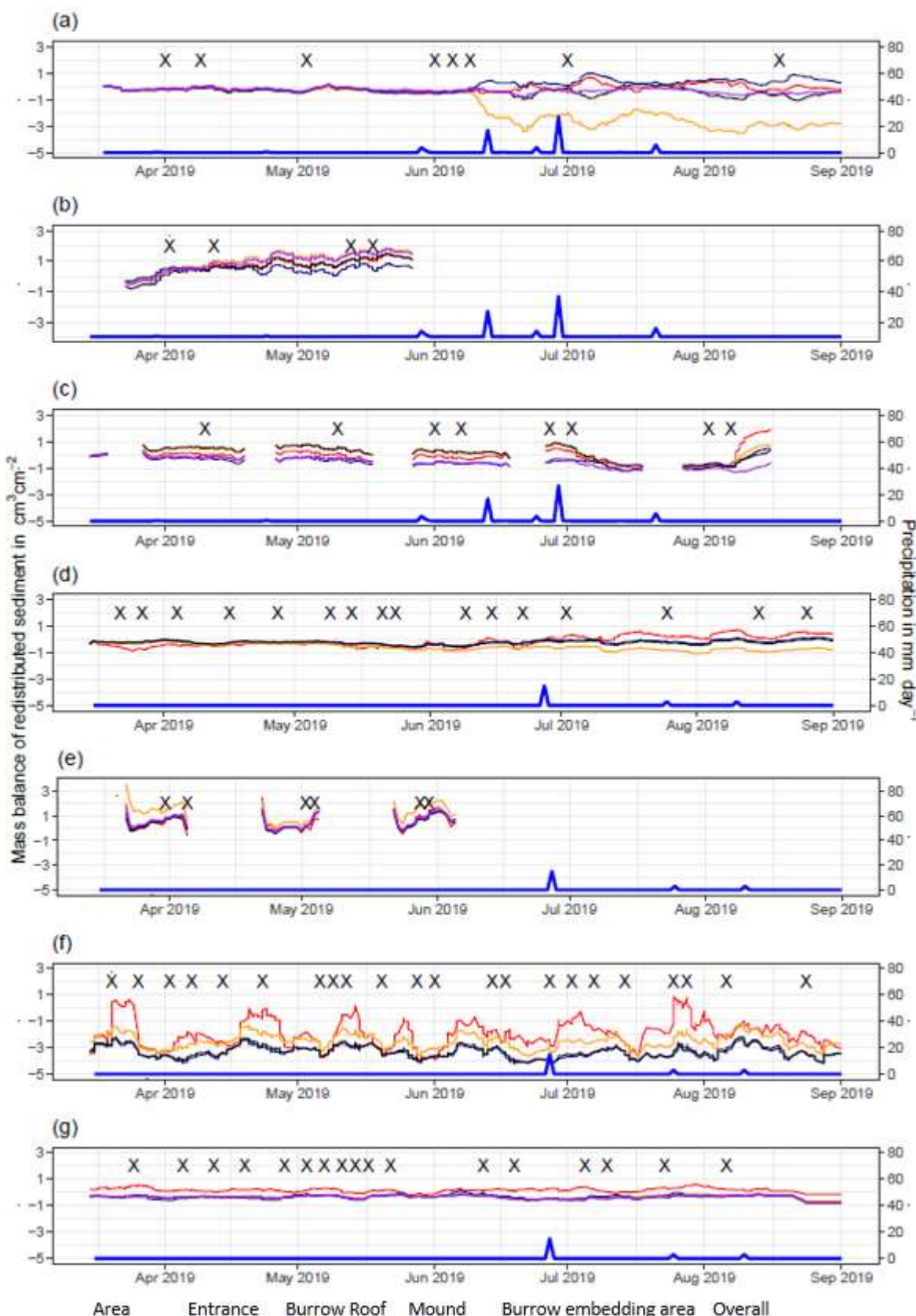


756
757 **Figure A3.** a) Estimation of Time-of-Flight camera accuracy based on averaging two surface scans before and
758 after the sediment extraction under controlled conditions. The x-axis shows the exact sediment volume
759 measured with a cup. The y-axis represents the volume of the sediment calculated from the camera scans
760 (according to Equation (4)). The blue line is the linear regression calculated from the measured and detected
761 volume. The green shadow shows the confidence interval of 95% for the linear regression slope. $^{***}p \leq 0.001$.
762 MAE is the mean absolute error, SD is standard deviation and R^2 the coefficient of determination. b) Measured
763 sediment volume subtracted from the detected sediment volume for all measurements.
764



765

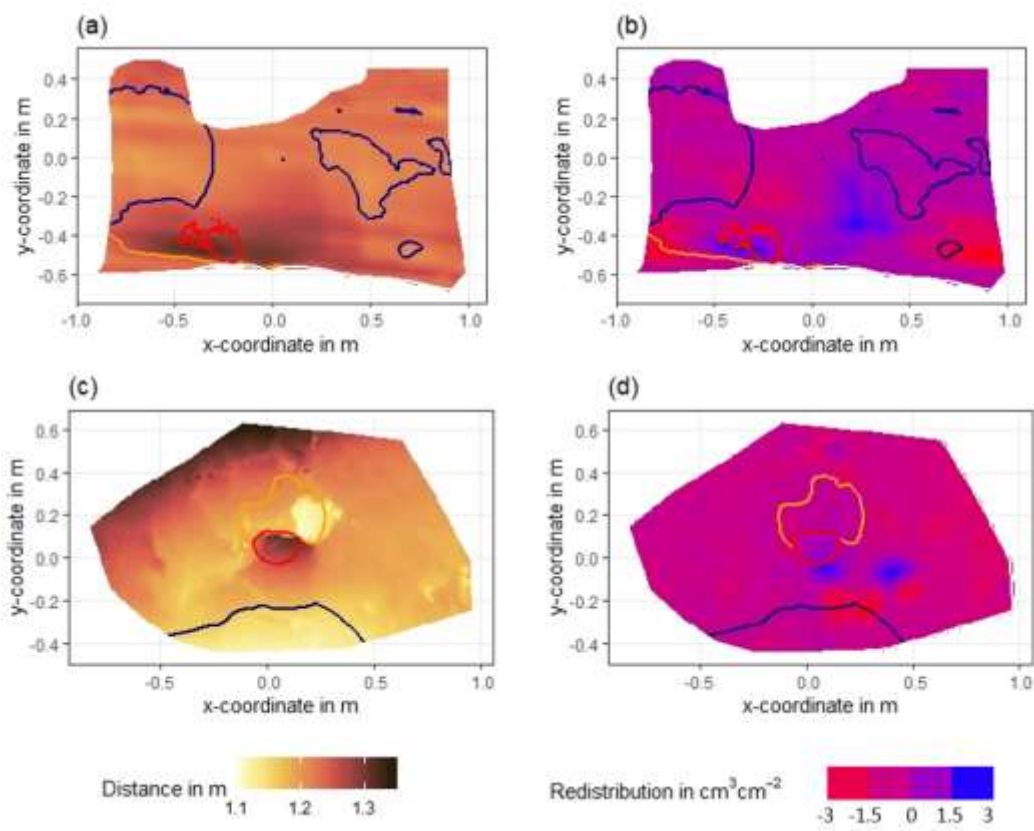
766 **Figure A4.** Sediment mass balance for the period of 7 months separately for burrows and burrow embedding
 767 areas as measured by the cameras. (a) LC-NU. (b) LC-SU. (c) LC-SL. (d) PdA-NU. (e) PdA-NL.
 768 (f) PdA-SU. (g) PdA-SL. For abbreviations see Table A1.



769

770 **Figure A5.** Sediment mass balance for the period of 7 months separately for all delineated areas as measured
771 by the cameras. (a) LC-NU. (b) LC-SU. (c) LC-SL. (d) PdA-NU. (e) PdA-NL. (f) PdA-SU. (g) PdA-SL. For
772 abbreviations see Table A1.

773

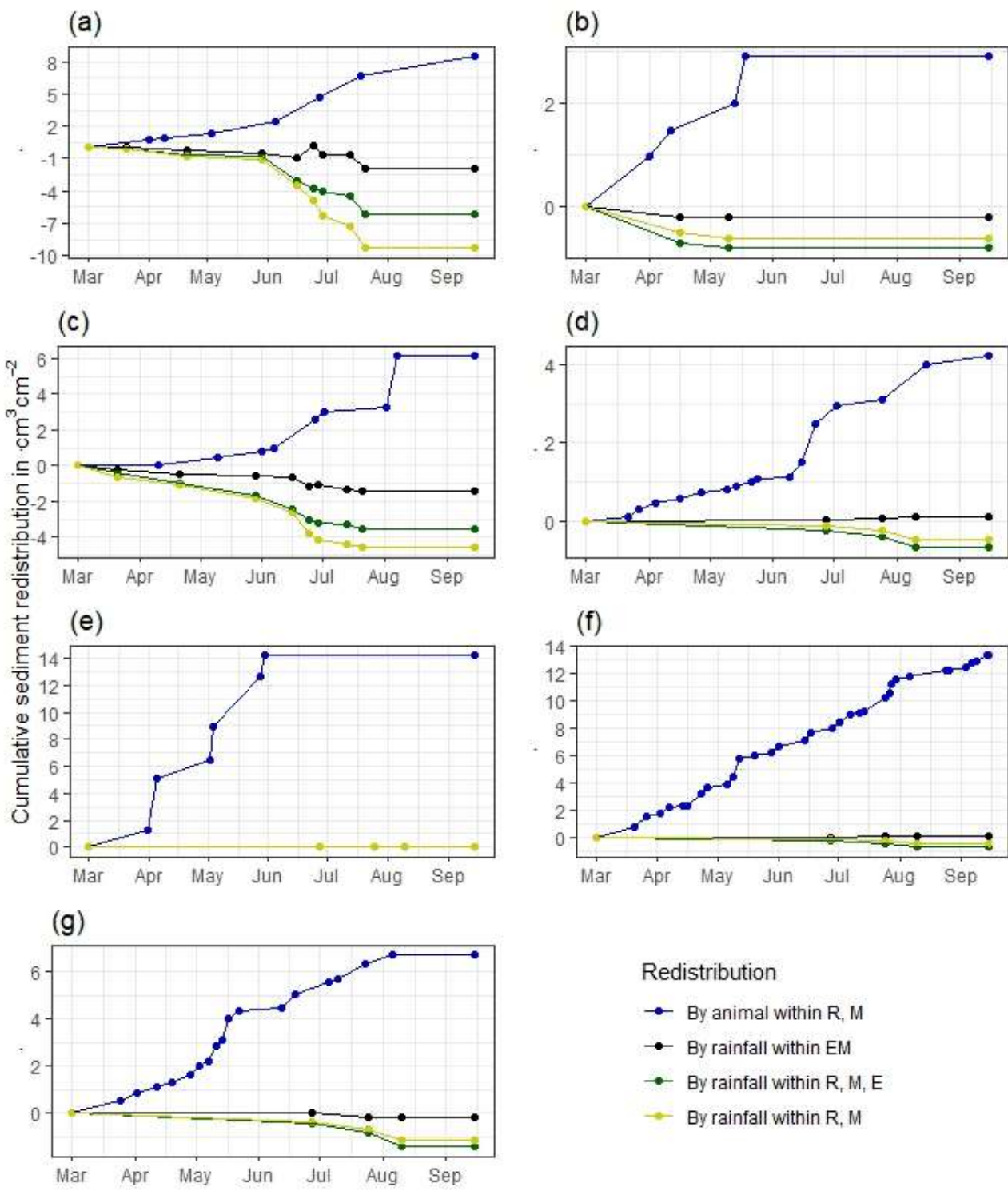


774

775 **Figure A6.** Examples of surface scans showing the digital surface model (DSM) before a rainfall event (a, c)
 776 at two camera locations in La Campana, and the calculated volume of redistributed sediment (b, d) after the
 777 rainfall event: (a) DSM of a scan from the camera on the upper north-facing hillslope in La Campana; (b)
 778 Detected sediment redistribution ($\text{cm}^3 \text{cm}^{-2}$) on the upper north-facing hillslope in La Campana after a rainfall
 779 event of 17.2 mm day^{-1} ; (c) DSM of a scan from the camera on the upper south-facing hillslope in La Campana;
 780 (d) Detected sediment redistribution ($\text{cm}^3 \text{cm}^{-2}$) on the upper south-facing hillslope after a rainfall event of 17.2
 781 mm day^{-1} . Red is the outline of the burrow entrance. Green is the outline of mound. Orange is the outline of
 782 the burrow roof. The area which is not outlined is burrow embedding area. Redistribution is the volume of the
 783 redistributed sediment, either accumulated (positive value) or eroded (negative value) per $\text{cm}^3 \text{cm}^{-2}$. After the
 784 rainfall events, sediment mostly accumulated within the burrow entrance or near mounds and eroded from
 785 burrow roofs and mounds.

786

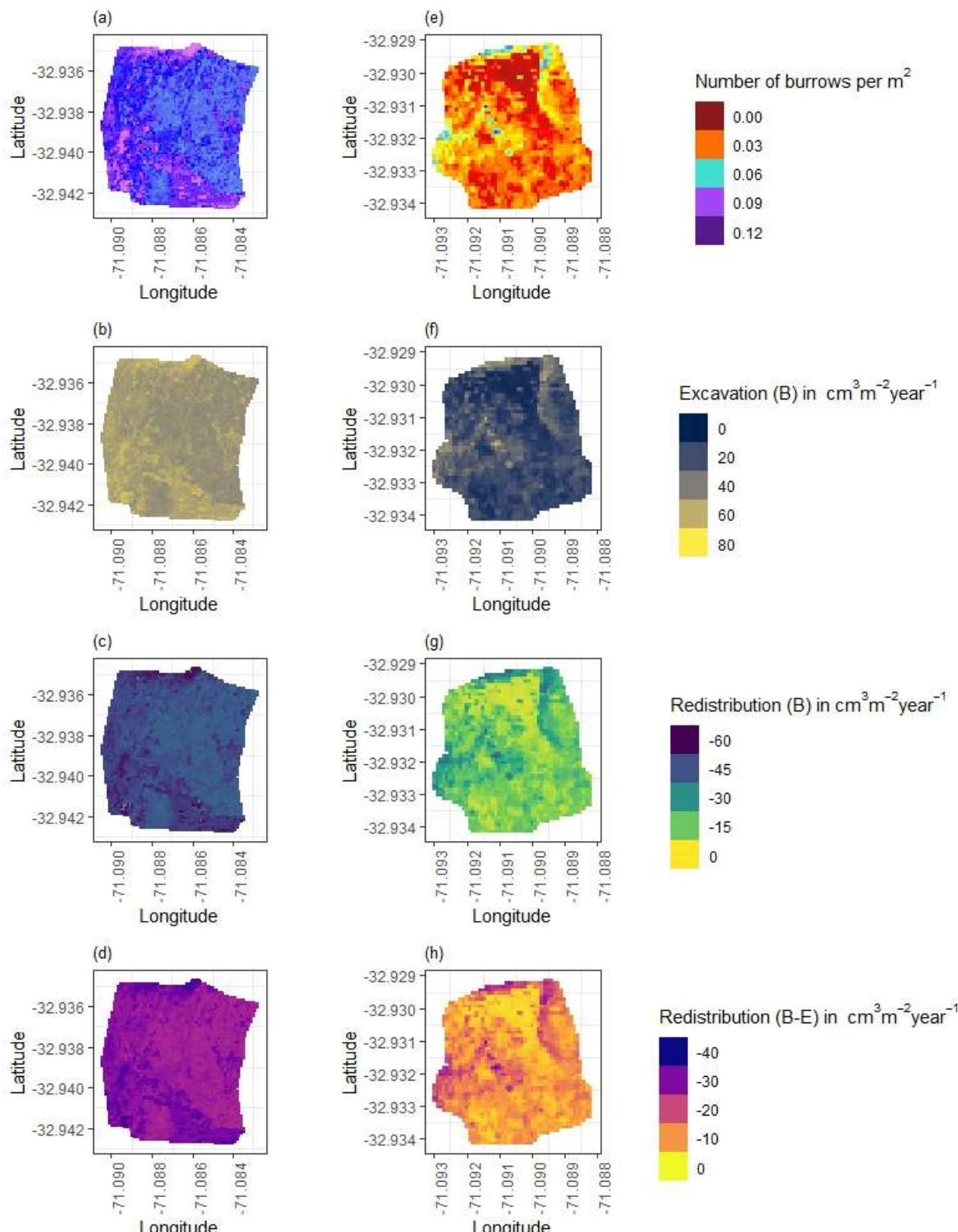
787



788

789 **Figure A7.** Cumulative volume of redistributed sediment for all cameras. Positive values indicate sediment
 790 accumulation. Negative values indicate sediment erosion. Whiskers are the median sediment redistribution. E
 791 is the burrow entrance. M is the mound. R is burrow roof. EM is burrow embedding area. LC is mediterranean
 792 climate zone. PdA is arid climate zone. (a) LC-NU. (b) LC-SU. (c) LC-SL. (d) PdA-NU. (e) PdA-NL. (f) PdA-
 793 SU. (g) PdA-SL. For abbreviations see Table A1.

794

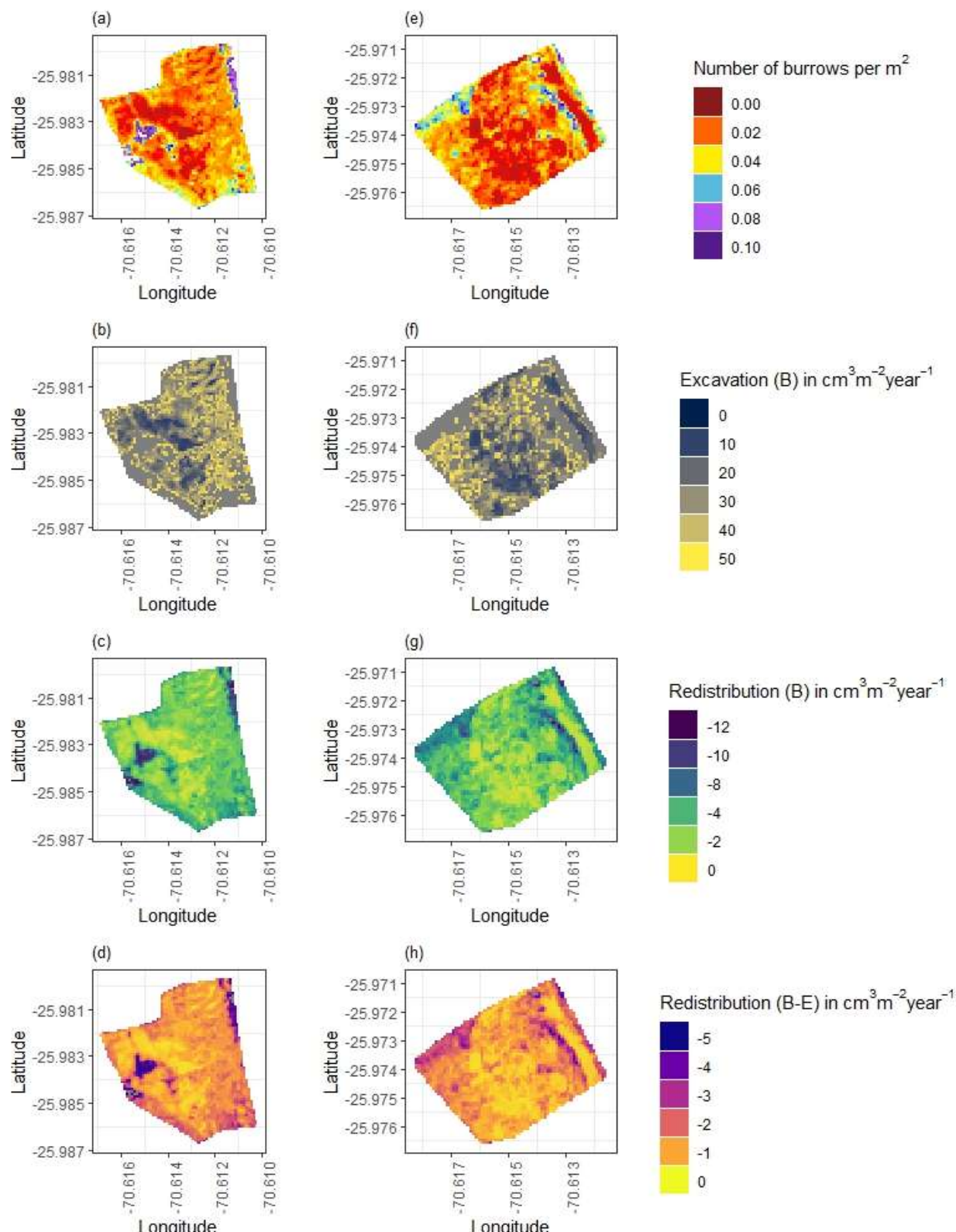


795

796 **Figure A8.** Hillslope-wide volume of redistributed sediment for a time period of one year in LC. (a-d) North-
797 facing hillslope. (e-h) South-facing hillslope. (a) and (e) Density of burrows as estimated by Grigusova et al.
798 2021. (b) and (f) Volume of the sediment excavated by the animals. (c) and (g) Volume of the sediment
799 redistributed during rainfall events within burrows. (d) and (h) Volume of additionally redistributed sediment
800 during rainfall events due to presence of the burrows. The values were calculated per burrow as stated in
801 section 3.7 by subtracting the sediment volume redistributed within burrows from the sediment volume

802 redistributed within burrow embedding area and then upscaled. B stays for burrow
803 embedding area.

804



805

806 **Figure A9.** Hillslope-wide volume of redistributed sediment for a time period of one year in Pan de Azúcar. (a-
807 d) North-facing hillslope. (e-h) South-facing hillslope. (a) and (e) Density of burrows as estimated by Grigusova
808 et al. 2021. (b) and (f) Volume of the sediment excavated by the animals. (c) and (g) Volume of the sediment
809 redistributed during rainfall events within burrows. (d) and (h) Volume of additionally redistributed sediment

810 during rainfall events due to presence of the burrows. The values were calculated per burrow as stated in
811 section 3.7 by subtracting the sediment volume redistributed within burrow from the sediment volume
812 redistributed within burrow embedding area and then upscaled. B stays for burrow, EM stays for burrow
813 embedding area by the burrowing animal.

814

815 Literaturverzeichnis

816 Afana, A.; Solé-Benet, A.; Pérez, J. L. (2010): Determination of Soil Erosion Using Laser Scanners.
817 Experimental Station of Arid Zone, CSIC, Almeria, Spain, zuletzt geprüft am 22.12.2021.

818 Andersen, Douglas C. (1987): Geomys Bursarius Burrowing Patterns: Influence of Season and
819 Food Patch Structure. In: *Ecology* 68 (5), S. 1306–1318. DOI: 10.2307/1939215.

820 Ashcroft, Michael B.; Gollan, John R.; Ramp, Daniel (2014): Creating vegetation density profiles
821 for a diverse range of ecological habitats using terrestrial laser scanning. In: *Methods Ecol Evol*
822 5 (3), S. 263–272. DOI: 10.1111/2041-210X.12157.

823 BANCROFT, W. J.; HILL, D.; ROBERTS, J. D. (2004): A new method for calculating volume of
824 excavated burrows: the geomorphic impact of Wedge-Tailed Shearwater burrows on Rottnest
825 Island. In: *Funct Ecology* 18 (5), S. 752–759. DOI: 10.1111/j.0269-8463.2004.00898.x.

826 Bernhard, Nadine; Moskwa, Lisa-Marie; Schmidt, Karsten; Oeser, Ralf A.; Aburto, Felipe; Bader,
827 Maaike Y. et al. (2018): Pedogenic and microbial interrelations to regional climate and local
828 topography: New insights from a climate gradient (arid to humid) along the Coastal Cordillera
829 of Chile. In: *CATENA* 170 (4), S. 335–355. DOI: 10.1016/j.catena.2018.06.018.

830 Black, Thomas A.; Montgomery, David R. (1991): Sediment transport by burrowing mammals,
831 Marin County, California. In: *Earth Surf. Process. Landforms* 16 (2), S. 163–172. DOI:
832 10.1002/esp.3290160207.

833 Blanch, Xabier; Eltner, Anette; Guinau, Marta; Abellán, Antonio (2021): Multi-Epoch and Multi-
834 Imagery (MEMI) Photogrammetric Workflow for Enhanced Change Detection Using Time-
835 Lapse Cameras. In: *Remote Sensing* 13 (8), S. 1460. DOI: 10.3390/rs13081460.

836 Castner, James L.; Fowler, H. G. (1984): Distribution of Mole Crickets (Orthoptera: Gryllotalpidae:
837 Scapteriscus) and the Mole Cricket Parasitoid Larra bicolor (Hymenoptera: Sphecidae) in Puerto
838 Rico. In: *The Florida Entomologist* 67 (3), S. 481. DOI: 10.2307/3494730.

839 Chen, Mingyu; Ma, Li; Shao, Ming'an; Wei, Xiaorong; Jia, Yuhua; Sun, Shuchen et al. (2021):
840 Chinese zokor (*Myospalax fontanieri*) excavating activities lessen runoff but facilitate soil
841 erosion – A simulation experiment. In: *CATENA* 202 (8), S. 105248. DOI:
842 10.1016/j.catena.2021.105248.

843 Coombes, Martin A. (2016): Biogeomorphology: diverse, integrative and useful. In: *Earth Surf.
844 Process. Landforms* 41 (15), S. 2296–2300. DOI: 10.1002/esp.4055.

845 Corenblit, Dov; Corbara, Bruno; Steiger, Johannes (2021): Biogeomorphological eco-evolutionary
846 feedback between life and geomorphology: a theoretical framework using fossorial mammals.
847 In: *Die Naturwissenschaften* 108 (6), S. 55. DOI: 10.1007/s00114-021-01760-y.

848 Eitel, Jan U.H.; Williams, C. Jason; Vierling, Lee A.; Al-Hamdan, Osama Z.; Pierson, Frederick B.
849 (2011): Suitability of terrestrial laser scanning for studying surface roughness effects on
850 concentrated flow erosion processes in rangelands. In: *CATENA* 87 (3), S. 398–407. DOI:
851 10.1016/j.catena.2011.07.009.

852 Eltner, A.; Mulsow, C.; Maas, H.-G. (2013): QUANTITATIVE MEASUREMENT OF SOIL
853 EROSION FROM TLS AND UAV DATA. In: *Int. Arch. Photogramm. Remote Sens. Spatial Inf.
854 Sci.* XL-1/W2, S. 119–124. DOI: 10.5194/isprsarchives-XL-1-W2-119-2013.

855 Eltner, A.; Schneider, D.; Maas, H.-G. (2016a): INTEGRATED PROCESSING OF HIGH
856 RESOLUTION TOPOGRAPHIC DATA FOR SOIL EROSION ASSESSMENT
857 CONSIDERING DATA ACQUISITION SCHEMES AND SURFACE PROPERTIES. In: *Int.
858 Arch. Photogramm. Remote Sens. Spatial Inf. Sci.* XLI-B5, S. 813–819. DOI:

859 10.5194/isprsarchives-XLI-B5-813-2016.

860 Eltner, Anette; Kaiser, Andreas; Abellan, Antonio; Schindewolf, Marcus (2017): Time lapse
861 structure-from-motion photogrammetry for continuous geomorphic monitoring. In: *Earth Surf.
862 Process. Landforms* 42 (14), S. 2240–2253. DOI: 10.1002/esp.4178.

863 Eltner, Anette; Kaiser, Andreas; Castillo, Carlos; Rock, Gilles; Neugirg, Fabian; Abellán, Antonio
864 (2016b): Image-based surface reconstruction in geomorphometry – merits, limits and
865 developments. In: *Earth Surf. Dynam.* 4 (2), S. 359–389. DOI: 10.5194/esurf-4-359-2016.

866 Gabet, Emmanuel J.; Reichman, O. J.; Seabloom, Eric W. (2003): The Effects of Bioturbation on
867 Soil Processes and Sediment Transport. In: *Annu. Rev. Earth Planet. Sci.* 31 (1), S. 249–273.
868 DOI: 10.1146/annurev.earth.31.100901.141314.

869 Galland, Olivier; Bertelsen, Håvard S.; Guldstrand, Frank; Girod, Luc; Johannessen, Rikke F.;
870 Bjøgger, Fanny et al. (2016): Application of open-source photogrammetric software MicMac for
871 monitoring surface deformation in laboratory models. In: *J. Geophys. Res. Solid Earth* 121 (4),
872 S. 2852–2872. DOI: 10.1002/2015JB012564.

873 Grigusova, Paulina; Larsen, Annegret; Achilles, Sebastian; Klug, Alexander; Fischer, Robin; Kraus,
874 Diana et al. (2021): Area-Wide Prediction of Vertebrate and Invertebrate Hole Density and
875 Depth across a Climate Gradient in Chile Based on UAV and Machine Learning. In: *Drones* 5
876 (3), S. 86. DOI: 10.3390/drones5030086.

877 Hakonson, T. E. (1999): The Effects of Pocket Gopher Burrowing on Water Balance and Erosion
878 from Landfill Covers. In: *J. environ. qual.* 28 (2), S. 659–665. DOI:
879 10.2134/jeq1999.00472425002800020033x.

880 Hall, Kevin; Boelhouwers, Jan; Driscoll, Kevin (1999): Animals as Erosion Agents in the Alpine
881 Zone: Some Data and Observations from Canada, Lesotho, and Tibet. In: *Arctic, Antarctic, and
882 Alpine Research* 31 (4), S. 436–446. DOI: 10.1080/15230430.1999.12003328.

883 Hancock, Greg; Lowry, John (2021): Quantifying the influence of rainfall, vegetation and animals
884 on soil erosion and hillslope connectivity in the monsoonal tropics of northern Australia. In:
885 *Earth Surf. Process. Landforms* 46 (10), S. 2110–2123. DOI: 10.1002/esp.5147.

886 Hänsel, Phoebe; Schindewolf, Marcus; Eltner, Anette; Kaiser, Andreas; Schmidt, Jürgen (2016):
887 Feasibility of High-Resolution Soil Erosion Measurements by Means of Rainfall Simulations
888 and SfM Photogrammetry. In: *Hydrology* 3 (4), S. 38. DOI: 10.3390/hydrology3040038.

889 Hazelhoff, L.; van Hoof, P.; Imeson, A. C.; Kwaad, F. J. P. M. (1981): The exposure of forest soil to
890 erosion by earthworms. In: *Earth Surf. Process. Landforms* 6 (3-4), S. 235–250. DOI:
891 10.1002/esp.3290060305.

892 Herbst, M.; Bennett, N. C. (2006): Burrow architecture and burrowing dynamics of the endangered
893 Namaqua dune mole rat (*Bathyergus janetta*) (Rodentia: Bathyergidae). In: *Journal of Zoology*
894 270 (3), S. 420–428. DOI: 10.1111/j.1469-7998.2006.00151.x.

895 Horn, B.K.P. (1981): Hill shading and the reflectance map. In: *Proc. IEEE* 69 (1), S. 14–47. DOI:
896 10.1109/PROC.1981.11918.

897 Imeson, A. C. (1977): Splash erosion, animal activity and sediment supply in a small forested
898 Luxembourg catchment. In: *Earth Surf. Process. Landforms* 2 (2-3), S. 153–160. DOI:
899 10.1002/esp.3290020207.

900 Imeson, A. C.; Kwaad, F. J. P. M. (1976): Some Effects of Burrowing Animals on Slope Processes
901 in the Luxembourg Ardennes. In: *Geografiska Annaler: Series A, Physical Geography* 58 (4), S.
902 317–328. DOI: 10.1080/04353676.1976.11879941.

903 Iserloh, T.; Ries, J. B.; Arnáez, J.; Boix-Fayos, C.; Butzen, V.; Cerdà, A. et al. (2013): European
904 small portable rainfall simulators: A comparison of rainfall characteristics. In: *CATENA* 110 (2),
905 S. 100–112. DOI: 10.1016/j.catena.2013.05.013.

906 James, M. R.; Robson, S. (2014): Sequential digital elevation models of active lava flows from
907 ground-based stereo time-lapse imagery. In: *ISPRS Journal of Photogrammetry and Remote
908 Sensing* 97 (3), S. 160–170. DOI: 10.1016/j.isprsjprs.2014.08.011.

909 Jones, Clive G.; Gutiérrez, Jorge L.; Byers, James E.; Crooks, Jeffrey A.; Lambrinos, John G.;
910 Talley, Theresa S. (2010): A framework for understanding physical ecosystem engineering by

911 organisms. In: *Oikos* 119 (12), S. 1862–1869. DOI: 10.1111/j.1600-0706.2010.18782.x.
912 Kaiser, Andreas; Neugirg, Fabian; Rock, Gilles; Müller, Christoph; Haas, Florian; Ries, Johannes;
913 Schmidt, Jürgen (2014): Small-Scale Surface Reconstruction and Volume Calculation of Soil
914 Erosion in Complex Moroccan Gully Morphology Using Structure from Motion. In: *Remote*
915 *Sensing* 6 (8), S. 7050–7080. DOI: 10.3390/rs6087050.

916 Kinlaw, A.; Grasmueck, M. (2012): Evidence for and geomorphologic consequences of a reptilian
917 ecosystem engineer: The burrowing cascade initiated by the Gopher Tortoise. In:
918 *Geomorphology* 157–158 (4), S. 108–121. DOI: 10.1016/j.geomorph.2011.06.030.

919 Kromer, Ryan; Walton, Gabe; Gray, Brian; Lato, Matt; Group, Robert (2019): Development and
920 Optimization of an Automated Fixed-Location Time Lapse Photogrammetric Rock Slope
921 Monitoring System. In: *Remote Sensing* 11 (16), S. 1890. DOI: 10.3390/rs11161890.

922 Kukko, Antero; Hyypää, Juha (2009): Small-footprint Laser Scanning Simulator for System
923 Validation, Error Assessment, and Algorithm Development. In: *photogramm eng remote sensing*
924 75 (10), S. 1177–1189. DOI: 10.14358/PERS.75.10.1177.

925 Larsen, A.; Nardin, W.; Lageweg, W. I.; Bätz, N. (2021): Biogeomorphology, quo vadis? On
926 processes, time, and space in biogeomorphology. In: *Earth Surf. Process. Landforms* 46 (1), S.
927 12–23. DOI: 10.1002/esp.5016.

928 Le Hir, P.; Monbet, Y.; Orvain, F. (2007): Sediment erodability in sediment transport modelling:
929 Can we account for biota effects? In: *Continental Shelf Research* 27 (8), S. 1116–1142. DOI:
930 10.1016/j.csr.2005.11.016.

931 Lehnert, Lukas W.; Thies, Boris; Trachte, Katja; Achilles, Sebastian; Osses, Pablo; Baumann, Karen
932 et al. (2018): A Case Study on Fog/Low Stratus Occurrence at Las Lomitas, Atacama Desert
933 (Chile) as a Water Source for Biological Soil Crusts. In: *Aerosol Air Qual. Res.* 18 (1), S. 254–
934 269. DOI: 10.4209/aaqr.2017.01.0021.

935 Li, Guorong; Li, Xilai; Li, Jinfang; Chen, Wenting; Zhu, Haili; Zhao, Jianyun; Hu, Xiasong
936 (2019a): Influences of Plateau Zokor Burrowing on Soil Erosion and Nutrient Loss in Alpine
937 Meadows in the Yellow River Source Zone of West China. In: *Water* 11 (11), S. 2258. DOI:
938 10.3390/w1112258.

939 Li, Larry (2014): Time-of-Flight Camera – An Introduction. Technical White Paper. Hg. v. Texas
940 Instruments. Online verfügbar unter <https://www.ti.com/lit/wp/sloa190b/sloa190b.pdf>, zuletzt
941 geprüft am 22.12.2021.

942 Li, T. C.; Shao, M. A.; Jia, Y. H.; Jia, X. X.; Huang, L. M.; Gan, M. (2019b): Small - scale
943 observation on the effects of burrowing activities of ants on soil hydraulic processes. In: *Eur J*
944 *Soil Sci* 70 (2), S. 236–244. DOI: 10.1111/ejss.12748.

945 Li, Tongchuan; Jia, Yuhua; Shao, Ming'an; Shen, Nan (2019c): Camponotus japonicus burrowing
946 activities exacerbate soil erosion on bare slopes. In: *Geoderma* 348 (4), S. 158–167. DOI:
947 10.1016/j.geoderma.2019.04.035.

948 Li, Tongchuan; Shao, Ming'an; Jia, Yuhua; Jia, Xiaoxu; Huang, Laiming (2018): Small-scale
949 observation on the effects of the burrowing activities of mole crickets on soil erosion and
950 hydrologic processes. In: *Agriculture, Ecosystems & Environment* 261 (4), S. 136–143. DOI:
951 10.1016/j.agee.2018.04.010.

952 Longoni, Laura; Papini, Monica; Brambilla, Davide; Barazzetti, Luigi; Roncoroni, Fabio; Scaioni,
953 Marco; Ivanov, Vladislav (2016): Monitoring Riverbank Erosion in Mountain Catchments Using
954 Terrestrial Laser Scanning. In: *Remote Sensing* 8 (3), S. 241. DOI: 10.3390/rs8030241.

955 MALLALIEU, JOSEPH; CARRIVICK, JONATHAN L.; QUINCEY, DUNCAN J.; SMITH,
956 MARK W.; JAMES, WILLIAM H.M. (2017): An integrated Structure-from-Motion and time-
957 lapse technique for quantifying ice-margin dynamics. In: *J. Glaciol.* 63 (242), S. 937–949. DOI:
958 10.1017/jog.2017.48.

959 Meysman, Filip J. R.; Boudreau, Bernard P.; Middelburg, Jack J. (2003): Relations between local,
960 nonlocal, discrete and continuous models of bioturbation. In: *Journal of Marine Research* 61
961 (3), S. 391–410. DOI: 10.1357/002224003322201241.

962 Morris, Rowena H.; Buckman, Solomon; Connelly, Paul; Dragovich, Deirdre; Ostendorf, Bertram;

963 and Bradstock, Ross A. (2011): The dirt on assessing post-fire erosion in the Mount Lofty
964 Ranges: comparing methods.

965 Nasermoaddeli, M. B.; Pasche, E. (2008): Application of terrestrial 3D scanner in quantification of
966 the riverbank erosion and deposition. Institute of river and coastal engineering, Technical
967 university Hamburg-Harburg, Hamburg,. Online verfügbar unter
968 [https://www.tuhh.de/t3resources/wb/Publikationen/MA-](https://www.tuhh.de/t3resources/wb/Publikationen/MA-Veroeffentlichungen/nasermoaddeli/riverflow2008.pdf)
969 Veroeffentlichungen/nasermoaddeli/riverflow2008.pdf, zuletzt geprüft am 22.12.2021.

970 Pang, Xiao Pan; Guo, Zheng Gang (2017): Plateau pika disturbances alter plant productivity and
971 soil nutrients in alpine meadows of the Qinghai-Tibetan Plateau, China. In: *Rangel. J.* 39 (2), S.
972 133. DOI: 10.1071/RJ16093.

973 Reichman, O. J.; Seabloom, Eric W. (2002): The role of pocket gophers as subterranean ecosystem
974 engineers. In: *Trends in Ecology & Evolution* 17 (1), S. 44–49. DOI: 10.1016/S0169-
975 5347(01)02329-1.

976 Richards, Paul J.; Humphreys, Geoff S. (2010): Burial and turbulent transport by bioturbation: a 27-
977 year experiment in southeast Australia. In: *Earth Surf. Process. Landforms* 21 (2), n/a-n/a. DOI:
978 10.1002/esp.2007.

979 Ridd, Peter V. (1996): Flow Through Animal Burrows in Mangrove Creeks. In: *Estuarine, Coastal
980 and Shelf Science* 43 (5), S. 617–625. DOI: 10.1006/ecss.1996.0091.

981 Romañach, Stephanie S.; Reichman, O. J.; Seabloom, E. W. (2005): Seasonal influences on
982 burrowing activity of a subterranean rodent, *Thomomys bottae*. In: *Journal of Zoology* 266 (3),
983 S. 319–325. DOI: 10.1017/S0952836905006941.

984 Rutin, J. (1996): The burrowing activity of scorpions (*Scorpio maurus palmatus*) and their potential
985 contribution to the erosion of Hamra soils in Karkur, central Israel. In: *Geomorphology* 15 (2),
986 S. 159–168. DOI: 10.1016/0169-555X(95)00120-T.

987 Sarbolandi, Hamed; Plack, Markus; Kolb, Andreas (2018): Pulse Based Time-of-Flight Range
988 Sensing. In: *Sensors (Basel, Switzerland)* 18 (6). DOI: 10.3390/s18061679.

989 Schiffers, Katja; Teal, Lorna Rachel; Travis, Justin Mark John; Solan, Martin (2011): An open
990 source simulation model for soil and sediment bioturbation. In: *PloS one* 6 (12), e28028. DOI:
991 10.1371/journal.pone.0028028.

992 Sharon, David (1980): The distribution of hydrologically effective rainfall incident on sloping
993 ground. In: *Journal of Hydrology* 46 (1-2), S. 165–188. DOI: 10.1016/0022-1694(80)90041-4.

994 Thomsen, L. M.; Baartman, J. E. M.; Barneveld, R. J.; Starkloff, T.; Stolte, J. (2015): Soil surface
995 roughness: comparing old and new measuring methods and application in a soil erosion model.
996 In: *SOIL* 1 (1), S. 399–410. DOI: 10.5194/soil-1-399-2015.

997 Übernickel, Kirstin; Ehlers, Todd A.; Paulino, Leandro; Fuentes Espoz, Juan-Pablo (2021a): Time
998 series of meteorological stations on an elevational gradient in National Park La Campana, Chile.
999 Unter Mitarbeit von Kirstin Übernickel, Todd A. Ehlers, Leandro Paulino, Juan-Pablo Fuentes
1000 Espoz, Ramiro Bernales-Noguera, Willi Kappler et al.

1001 Übernickel, Kirstin; Pizarro-Araya, Jaime; Bhagavathula, Susila; Paulino, Leandro; Ehlers, Todd A.
1002 (2021b): Reviews and syntheses: Composition and characteristics of burrowing animals along a
1003 climate and ecological gradient, Chile. In: *Biogeosciences* 18 (20), S. 5573–5594. DOI:
1004 10.5194/bg-18-5573-2021.

1005 Voiculescu, Mircea; Ianăş, Ana-Neli; Germain, Daniel (2019): Exploring the impact of snow vole
1006 (*Chionomys nivalis*) burrowing activity in the Făgăraş Mountains, Southern Carpathians
1007 (Romania): Geomorphic characteristics and sediment budget. In: *CATENA* 181 (1), S. 104070.
1008 DOI: 10.1016/j.catena.2019.05.016.

1009 Wei, Xinghu; Li, Sen; Yang, Ping; Cheng, Huaishun (2007): Soil erosion and vegetation succession
1010 in alpine Kobresia steppe meadow caused by plateau pika—A case study of Nagqu County,
1011 Tibet. In: *Chin. Geograph. Sc.* 17 (1), S. 75–81. DOI: 10.1007/s11769-007-0075-0.

1012 Wilkinson, Marshall T.; Richards, Paul J.; Humphreys, Geoff S. (2009): Breaking ground:
1013 Pedological, geological, and ecological implications of soil bioturbation. In: *Earth-Science
1014 Reviews* 97 (1-4), S. 257–272. DOI: 10.1016/j.earscirev.2009.09.005.

1015 Yair, A. (1995): Short and long term effects of bioturbation on soil erosion, water resources and soil
1016 development in an arid environment. In: *Geomorphology* 13 (1-4), S. 87–99. DOI:
1017 10.1016/0169-555X(95)00025-Z.

1018 Yáñez, E.; Barbieri, M.A.; Silva, C.; Nieto, K.; Espíndola, F. (2001): Climate variability and pelagic
1019 fisheries in northern Chile. In: *Progress in Oceanography* 49 (1-4), S. 581–596. DOI:
1020 10.1016/S0079-6611(01)00042-8.

1021 Yoo, Kyungsoo; Amundson, Ronald; Heimsath, Arjun M.; Dietrich, William E. (2005): Process-
1022 based model linking pocket gopher (*Thomomys bottae*) activity to sediment transport and soil
1023 thickness. In: *Earth Surf. Process. Landforms* 33 (11), S. 917. DOI: 10.1130/G21831.1.
1024

1025